High-Order Fully Coupled Scheme Based on Compact Integrated RBF Approximation for Viscous Flows in Regular and Irregular Domains

C.M.T. Tien[1], N. Thai-Quang[1], N. Mai-Duy[1], C.-D. Tran[1] and T. Tran-Cong[1]

Abstract: In this study, we present a numerical discretisation scheme, based on a direct fully coupled approach and compact integrated radial basis function (CIRBF) approximations, to simulate viscous flows in regular/irregular domains. The governing equations are taken in the primitive form where the velocity and pressure fields are solved in a direct fully coupled approach. Compact local approximations, based on integrated radial basis functions, over 3-node stencils are introduced into the direct fully coupled approach to represent the field variables. The present scheme is verified through the solutions of several problems including Poisson equations, Taylor-Green vortices and lid driven cavity flows, defined on domains of different shapes. The numerical results obtained by the present scheme are highly accurate and in good agreement with those reported in earlier studies of the same problems.

Keywords: Compact integrated RBF, fully coupled approach, regular/irregular domains, viscous flow, Poisson equations, Taylor-Green vortices, lid driven cavity.

1 Introduction

In the primitive variable discrete formulation of the incompressible Navier-Stokes equations, the treatment of the velocity-pressure coupling has a major influence on the convergence rate of the fluid flow simulation. In the incompressible Navier-Stokes equations, the pressure appears only through its gradient in the momentum equations and is only indirectly specified via the continuity equation. The lack of a dedicated equation for the pressure causes difficulty in solving the incompressible Navier-Stokes equations. Numerous approaches of coupling between the velocity and pressure fields have been studied to overcome this problem in the past decades.

---

[1] Computational Engineering and Science Research Centre, Faculty of Health, Engineering and Sciences, The University of Southern Queensland, Toowoomba, Queensland 4350, Australia.

There are generally two approaches for the issue of the velocity-pressure storage and coupling: segregated approaches and fully coupled approaches.

The segregated approach, in which the continuity and momentum equations are solved sequentially, leads the most often to a so-called pressure correction method. The first attempt of the segregated method was introduced by Patankar and Spalding (1972), in which the pressure field is determined by two processes: first computing an intermediate field based on a guessed pressure field; then conducting a correction process to ensure the new velocity satisfies the continuity equation. A difficulty of this approach lies in the lack of a pressure time derivative term in the continuity equation. Several methods have been proposed to overcome this drawback and they are classified by the way in which the incompressibility constraint is imposed. Among them, the commonly used methods are the so called pressure based schemes in which the velocity-pressure coupling is solved iteratively. The velocity variables are updated in the momentum equations and the pressure fields are computed in pressure equations. The updating procedure is processed by the well-known SIMPLE (Semi-Implicit Method for Pressure Linked Equations) or SIMPLEC (SIMPLE-Consistent) or SIMPLER (SIMPLE-Revisited) or PISO (Pressure-Implicit with Splitting of Operator) algorithm [Acharya, Baliga, Karki, Murthy, Prakash, and Vanka (2007)]. The algorithms improve the robustness of the pressure solver controlling its convergence rate and bring significant benefits for the overall method. However, the main shortcoming of these methods, where the velocity-pressure coupling is not enforced at each stage of iteration through the solution of the linearised system, is that the convergence slows down when the number of grid points increases [Deng, Piquet, Queutey, and Visonneau (1994a); Pascau and Perez (1996); Elman, Howle, Shadid, and Tuminario (2003); Ammara and Masson (2004); Darwish, Sraj, and Moukalled (2009)].

The fully coupled approach, in which the discretised equations of all variables are solved as one system, has been investigated as an alternative to the segregated approach. In these approaches, no explicit equation for pressure or for pressure correction is required and the momentum and continuity equations are discretised in a straightforward manner. Caretto, Curr, and Spalding (1972) proposed the coupled solution for the momentum equations and the continuity equation, the so-called SIVA (SImultaneous Variable Adjustments) algorithm. In this approach, the coupling between dependent variables is structured in small sub-domains. The resulting matrices in such approaches are easy to compute but poor convergence rates are obtained, due to the weak coupling between sub-domains, especially on fine grids. Multigrid methods [Vanka (1986a); Bruneau and Jouron (1990)] have been developed to overcome this problem; however, they do not appear to bring significant improvement in comparison with standard pressure based methods [Deng, Piquet,

Queutey, and Visonneau (1994a)]. Some other examples of the fully coupled algorithm include the SCGS (Symmetrical Coupled Gauss-Seidel) of Vanka (1986a), the UVP method of Karki and Mongia (1990), among others. The absence of a pressure equation in these fully coupled algorithms may lead to an ill-conditioned system of equations because zeros are present in the main diagonal of the discretised continuity equation [Darwish, Sraj, and Moukalled (2009)]. Attempts have been made to deal with this issue, with various degrees of success, through the use of preconditioning [May and Moresi (2008); Henniger, Obrist, and Kleiser (2010)], penalty methods [Braaten and Patankar (1990); Pascau and Perez (1996)], or by algebraic manipulations [Zedan and Schneider (1985); Galpin, Doormaal, and Raithby (1985)]. These treatments may improve the stiffness of equations. Mazhar (2001) presents a fully coupled approach differing from the aforementioned approaches in the sense that a direct attempt is made to solve the primitive difference equations.

In [Hanby, Silvester, and Chew (1996)], a fully coupled procedure is presented and compared with the SIMPLEC solver. The comparison shows that a fully coupled solution gives quicker convergence with less nonlinear (or outer) iteration. Braaten and Shyy (1986) investigated the effects of mesh skewness, Reynold number and grid size on the iterative and direct solution methods. The results show the fully coupled fully implicit treatment of equations in the direct sparse matrix method leads to rates of convergence that are much more rapid than the iterative method. The work also indicates the importance of retaining the coupling between velocity and pressure fields in obtaining the superior rate of convergence of the direct scheme. Whilst a fully coupled method requires more computer memory than a segregated approach, this is not a serious limitation on most current computers and it may offer advantages in terms of robustness, CPU time, and level of convergence.

Radial basis function networks (RBFNs) have emerged as a powerful numerical method for the approximation of scattered data [Fasshauer (2007)]. Kansa (1990a) and Kansa (1990b) first proposed the concept of using direct/differential RBF (DRBF) approximation for solving partial differential equations (PDEs). In the DRBF method, the closed form RBF approximating function is first obtained from a set of training points and the derivative functions are then calculated directly from such closed form RBF [Mai-Duy and Tran-Cong (2001a)]. Mai-Duy and Tran-Cong (2001b) and Mai-Duy and Tran-Cong (2003) then proposed the idea of using indirect/integrated RBF (IRBF) for the solution of PDEs. In the IRBF approach, the highest derivatives under interest are decomposed in to RBFs; the expressions for the lower derivatives and its functions are then obtained through integration processes. Numerical studies in [Mai-Duy and Tran-Cong (2001a); Mai-Duy and Tran-Cong (2001b); Mai-Duy and Tran-Cong (2003); Mai-Duy and Tran-Cong

(2005)] have shown that the integral approach is more accurate than the differential approach because the integration process is averagely less sensitive to noise. To employ a larger number of collocation points, a one-dimensional IRBF scheme has been developed in literatures [Mai-Duy and Tanner (2007); Mai-Duy and Tran-Cong (2007)]. Recently, Mai-Duy and Tran-Cong (2013) have proposed a 3-point compact IRBF (CIRBF) stencil where only nodal values of the second-order derivative (i.e. extra information) are incorporated into the approximations. Thai-Quang, Mai-Duy, Tran, and Tran-Cong (2012) has proposed another 3-point CIRBF stencil where the extra information includes nodal values of both the first- and second-order derivatives. The latter scheme with tri-diagonal matrices was reported to be more accurate and efficient [Thai-Quang, Mai-Duy, Tran, and Tran-Cong (2012)].

This article implements a direct fully coupled approach for the fluid flow simulation with the field variables being approximated on uniform/non-uniform Cartesian grids by the CIRBF approximation scheme presented in [Thai-Quang, Mai-Duy, Tran, and Tran-Cong (2012)]. The tight velocity-pressure coupling is developed on a collocated grid and one global system of equations involving the velocity and pressure is solved simultaneously in its primitive form. In this way, momentum and continuity conservation equations are satisfied implicitly and simultaneously over the whole grid points. The use of fully coupled fully implicit solver for Navier-Stokes equations exhibits rapid convergence and provides the stability for large time steps to be employed [Elman, Howle, Shadid, and Tuminario (2003)]. A block preconditioning technique [Henniger, Obrist, and Kleiser (2010)] is used to refine the direct solution only when the coefficient matrix is ill-conditioned (e.g. the problem of irregular bottom lid driven cavity).

The remainder of this paper is organised as follows: Section 2 outlines the governing equations and a fully coupled approach. Following this, a block preconditioning technique is briefly described in section 3. Section 4 describes the spatial disretisation using CIRBF stencils. In Section 5, numerical examples are presented and the CIRBF results are compared with some benchmark solutions, where appropriate. Finally, concluding remarks are given in Section 6.

2   Mathematical model

The transient Navier-Stokes equations for an incompressible viscous fluid in the primitive variables are expressed in the dimensionless non-conservative forms as follows.

Conservation of x-momentum

$$\frac{\partial u}{\partial t} + \underbrace{\left\{ u\frac{\partial u}{\partial x} + v\frac{\partial u}{\partial y} \right\}}_{N(u)} = -\frac{\partial p}{\partial x} + \frac{1}{Re}\underbrace{\left\{ \frac{\partial^2 u}{\partial x^2} + \frac{\partial^2 u}{\partial y^2} \right\}}_{L(u)}, \tag{1}$$

conservation of y-momentum

$$\frac{\partial v}{\partial t} + \underbrace{\left\{ u\frac{\partial v}{\partial x} + v\frac{\partial v}{\partial y} \right\}}_{N(v)} = -\frac{\partial p}{\partial y} + \frac{1}{Re}\underbrace{\left\{ \frac{\partial^2 v}{\partial x^2} + \frac{\partial^2 v}{\partial y^2} \right\}}_{L(v)}, \tag{2}$$

conservation of mass (continuity)

$$\frac{\partial u}{\partial x} + \frac{\partial v}{\partial y} = 0, \tag{3}$$

where u, v and p are the velocity components in the x-, y-direction and static pressure, respectively; $Re = Ul/v$ is the Reynolds number, in which v, l and U are the kinematic viscosity, characteristic length and characteristic speed of the flow, respectively. For simplicity, we employ notations $N(u)$ and $N(v)$ to represent the convective terms in x- and y-directions, respectively; and, $L(u)$ and $L(v)$ to denote the diffusive terms in x- and y-directions, respectively.

The temporal discretisations of (1)-(3), using the Adams-Bashforth scheme for the convective terms and Crank-Nicolson scheme for the diffusive terms, result in

$$\frac{u^n - u^{n-1}}{\Delta t} + \left\{ \frac{3}{2}N(u^{n-1}) - \frac{1}{2}N(u^{n-2}) \right\} = -G_x(p^{n-\frac{1}{2}}) + \frac{1}{2Re}\left\{ L(u^n) + L(u^{n-1}) \right\},$$
$$\tag{4}$$

$$\frac{v^n - v^{n-1}}{\Delta t} + \left\{ \frac{3}{2}N(v^{n-1}) - \frac{1}{2}N(v^{n-2}) \right\} = -G_y(p^{n-\frac{1}{2}}) + \frac{1}{2Re}\left\{ L(v^n) + L(v^{n-1}) \right\},$$
$$\tag{5}$$

$$D_x(u^n) + D_y(v^n) = 0, \tag{6}$$

where n denotes the current time level; G_x and G_y are gradients in x- and y-directions, respectively; and D_x and D_y are gradients in x- and y-directions, respectively.

Taking the unknown quantities in (4)-(6) to the left hand side and the known quantities to the right hand side, and then collocating them at the interior nodal points result in the matrix-vector form

$$\begin{bmatrix} \mathbf{K} & \mathbf{0} & \mathbf{G}_x \\ \mathbf{0} & \mathbf{K} & \mathbf{G}_y \\ \mathbf{D}_x & \mathbf{D}_y & \mathbf{0} \end{bmatrix} \begin{bmatrix} \mathbf{u}^n \\ \mathbf{v}^n \\ \mathbf{p}^{n-\frac{1}{2}} \end{bmatrix} = \begin{bmatrix} \mathbf{r}_x^n \\ \mathbf{r}_y^n \\ \mathbf{0} \end{bmatrix}, \tag{7}$$

where

$$\mathbf{K} = \frac{1}{\Delta t} \left\{ \mathbf{I} - \frac{\Delta t}{2Re} \mathbf{L} \right\}, \tag{8}$$

$$\mathbf{r}_x^n = \frac{1}{\Delta t} \left\{ \mathbf{I} + \frac{\Delta t}{2Re} \mathbf{L} \right\} \mathbf{u}^{n-1} - \left\{ \frac{3}{2} \mathbf{N}(\mathbf{u}^{n-1}) - \frac{1}{2} \mathbf{N}(\mathbf{u}^{n-2}) \right\}, \tag{9}$$

$$\mathbf{r}_y^n = \frac{1}{\Delta t} \left\{ \mathbf{I} + \frac{\Delta t}{2Re} \mathbf{L} \right\} \mathbf{v}^{n-1} - \left\{ \frac{3}{2} \mathbf{N}(\mathbf{v}^{n-1}) - \frac{1}{2} \mathbf{N}(\mathbf{v}^{n-2}) \right\}, \tag{10}$$

$\mathbf{u}^n$ and $\mathbf{v}^n$ are vectors containing the nodal values of u^n and v^n at the boundary and interior nodes, respectively, while $\mathbf{p}^{n-\frac{1}{2}}$ is a vector containing the values of $p^{n-\frac{1}{2}}$ at the interior nodes only; $\mathbf{I}$ is the identity matrix; and $\mathbf{N}$ and $\mathbf{L}$ are the matrix operators for the approximation of the convective and diffusive terms, respectively.

Since the velocities are given at the boundary, the goal of the fully coupled approach is to solve (7) for the values of the field variables simultaneously at the interior points. In (7), the approximation for the pressure involves the interior nodal points only. This is in accord with the fact that physics does not provide a prior boundary condition for pressure as it does for velocities [Moin and Kim (1980)]. It is noted that the pressure is only determined up to an arbitrary constant because there exists no direct equation for pressure and the momentum equations only contain gradient terms for pressure [Moin and Kim (1980); Vanka (1986b); Bruneau and Jouron (1990); Perot (1993); May and Moresi (2008)].

3 Preconditioning technique

For simplicity, we define

$$\widehat{\mathbf{K}} = \begin{bmatrix} \mathbf{K} & \mathbf{0} \\ \mathbf{0} & \mathbf{K} \end{bmatrix}, \ \ \mathbf{G} = \begin{bmatrix} \mathbf{G}_x \\ \mathbf{G}_y \end{bmatrix}, \ \ \mathbf{D} = \begin{bmatrix} \mathbf{D}_x & \mathbf{D}_y \end{bmatrix}, \ \ \mathbf{U}^n = \begin{bmatrix} \mathbf{u}^n \\ \mathbf{v}^n \end{bmatrix}, \ \ \mathbf{R}^n = \begin{bmatrix} \mathbf{r}_x^n \\ \mathbf{r}_y^n \end{bmatrix}. \tag{11}$$

Substituting (11) into (7)

$$\begin{bmatrix} \widehat{\mathbf{K}} & \mathbf{G} \\ \mathbf{D} & \mathbf{0} \end{bmatrix} \begin{bmatrix} \mathbf{U}^n \\ \mathbf{p}^{n-\frac{1}{2}} \end{bmatrix} = \begin{bmatrix} \mathbf{R}^n \\ \mathbf{0} \end{bmatrix}. \tag{12}$$

Block-oriented preconditioning methods for the Navier-Stokes equation decompose the block 2×2 matrix in (12) using a block-LU decomposition

$$\begin{bmatrix} \widehat{\mathbf{K}} & \mathbf{G} \\ \mathbf{D} & \mathbf{0} \end{bmatrix} = \begin{bmatrix} \mathbf{I} & \mathbf{0} \\ \mathbf{D}\widehat{\mathbf{K}}^{-1} & -\mathbf{I} \end{bmatrix} \begin{bmatrix} \widehat{\mathbf{K}} & \mathbf{G} \\ \mathbf{0} & \mathbf{D}\widehat{\mathbf{K}}^{-1}\mathbf{G} \end{bmatrix}. \tag{13}$$

By defining Schur complement as $\mathbf{S} = \mathbf{D}\widehat{\mathbf{K}}^{-1}\mathbf{G}$ [Silvester, Elman, Kay, and Wathen (2001)], the block upper triangular preconditioner is expressed as

$$\begin{bmatrix} \widehat{\mathbf{K}} & \mathbf{G} \\ \mathbf{0} & \mathbf{S} \end{bmatrix}. \tag{14}$$

Substituting (13) into (12), we can obtain the Schur complement for the pressure [May and Moresi (2008); Henniger, Obrist, and Kleiser (2010); Furuichi, May, and Tackley (2011)]. It yields the following block upper triangular system

$$\begin{bmatrix} \widehat{\mathbf{K}} & \mathbf{G} \\ \mathbf{0} & \mathbf{S} \end{bmatrix} \begin{bmatrix} \mathbf{U}^n \\ \mathbf{p}^{n-\frac{1}{2}} \end{bmatrix} = \begin{bmatrix} \mathbf{R}^n \\ \mathbf{F}^n \end{bmatrix}, \tag{15}$$

where $\mathbf{F}^n = \mathbf{D}\widehat{\mathbf{K}}^{-1}\mathbf{R}^n$.

The velocity and pressure solutions are obtained via block back substitution in (15), i.e. solving the following systems

$$\text{solve for } \mathbf{p}: \quad \mathbf{S}\mathbf{p}^{n-\frac{1}{2}} = \mathbf{F}^n. \tag{16}$$

$$\text{solve for } \mathbf{U}: \quad \widehat{\mathbf{K}}\mathbf{U}^n = \mathbf{R}^n - \mathbf{G}\mathbf{p}^{n-\frac{1}{2}}. \tag{17}$$

In this work, it is noted that the preconditioning technique is required whenever the coefficient matrix is ill-conditioned. In particular, it is only used to stiffen the coefficient matrix for the problem of an irregular bottom lid driven cavity in Section 5.6.

4 Spatial discretisation

For the approximation of the first- and second-order derivatives in (7), a compact IRBF (CIRBF) scheme of Thai-Quang, Mai-Duy, Tran, and Tran-Cong (2012) is employed in this paper. It is represented as follows.

Consider a two-dimensional domain Ω, which is represented by a uniform Cartesian grid. The nodes are indexed in the x-direction by the subscript i ($i \in \{1, 2, ..., n_x\}$) and in y-direction by j ($j \in \{1, 2, ..., n_y\}$). For rectangular domains, let N be the total number of nodes (i.e. $N = n_x \times n_y$) and N_{ip} be the number of interior nodes (i.e. $N_{ip} = (n_x - 2) \times (n_y - 2)$). For non-rectangular domains, selection of interior nodes is detailed in Section 5.2. At an interior grid point $\mathbf{x}_{i,j} = (x_{(i,j)}, y_{(i,j)})^T$ where $i \in \{2, 3, ..., n_x - 1\}$ and $j \in \{2, 3, ..., n_y - 1\}$, the associated stencils to be considered here are two local stencils: $\{x_{(i-1,j)}, x_{(i,j)}, x_{(i+1,j)}\}$ in the x-direction and $\{y_{(i,j-1)}, y_{(i,j)}, y_{(i,j+1)}\}$ in the y-direction. Hereafter, for brevity, η denotes either x or y in a generic local stencil $\{\eta_1, \eta_2, \eta_3\}$, where $\eta_1 < \eta_2 < \eta_3$ and $\eta_2 \equiv \eta_{(i,j)}$, are illustrated in Figure 1.
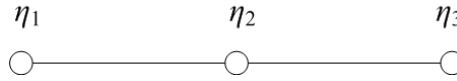
Figure 1: Compact 3-point 1D-IRBF stencil for interior nodes.

The integral approach starts with the decomposition of the second-order derivative of a variable, u, into RBFs

$$\frac{d^2 u(\eta)}{d\eta^2} = \sum_{i=1}^{m} w_i G_i(\eta), \tag{18}$$

where m is taken to be 3 for local stencils; $\{G_i(\eta)\}_{i=1}^{m}$ is the set of RBFs; and $\{w_i\}_{i=1}^{m}$ the set of weights/coefficients to be found. Approximate representations for the first-order derivative and the function itself are then obtained through the integration processes

$$\frac{du(\eta)}{d\eta} = \sum_{i=1}^{m} w_i H_i(\eta) + c_1, \tag{19}$$

$$u(\eta) = \sum_{i=1}^{m} w_i \overline{H}_i(\eta) + c_1 \eta + c_2, \tag{20}$$

where $H_i(\eta) = \int G_i(\eta)d\eta$; $\overline{H}_i(\eta) = \int H_i(\eta)d\eta$; c_1 and c_2 are the constants of integration.

4.1 First-order derivative compact approximations

Extra information used in the compact approximation of the first-order derivative is chosen as $\frac{du_1}{d\eta}$ and $\frac{du_3}{d\eta}$. We construct the conversion system over a 3-point stencil associated with an interior node in the form

$$\begin{bmatrix} u_1 \\ u_2 \\ u_3 \\ \frac{du_1}{d\eta} \\ \frac{du_3}{d\eta} \end{bmatrix} = \underbrace{\begin{bmatrix} \overline{\mathbf{H}} \\ \mathbf{H} \end{bmatrix}}_{\mathbf{C}_1} \begin{bmatrix} w_1 \\ w_2 \\ w_3 \\ c_1 \\ c_2 \end{bmatrix}, \tag{21}$$

where $\frac{du_i}{d\eta} = \frac{du}{d\eta}(\eta_i)$ with $i \in \{1,2,3\}$; $\mathbf{C}_1$ is the conversion matrix; $\overline{\mathbf{H}}$ and $\mathbf{H}$ are defined as

$$\overline{\mathbf{H}} = \begin{bmatrix} \overline{H}_1(\eta_1) & \overline{H}_2(\eta_1) & \overline{H}_3(\eta_1) & \eta_1 & 1 \\ \overline{H}_1(\eta_2) & \overline{H}_2(\eta_2) & \overline{H}_3(\eta_2) & \eta_2 & 1 \\ \overline{H}_1(\eta_3) & \overline{H}_2(\eta_3) & \overline{H}_3(\eta_3) & \eta_3 & 1 \end{bmatrix}. \tag{22}$$

$$\mathbf{H} = \begin{bmatrix} H_1(\eta_1) & H_2(\eta_1) & H_3(\eta_1) & 1 & 0 \\ H_1(\eta_3) & H_2(\eta_3) & H_3(\eta_3) & 1 & 0 \end{bmatrix}. \tag{23}$$

Solving (21) yields

$$\begin{bmatrix} w_1 \\ w_2 \\ w_3 \\ c_1 \\ c_2 \end{bmatrix} = \mathbf{C}_1^{-1} \begin{bmatrix} u_1 \\ u_2 \\ u_3 \\ \frac{du_1}{d\eta} \\ \frac{du_3}{d\eta} \end{bmatrix}, \tag{24}$$

which maps the vector of nodal values of the function and its first-order derivative to the vector of RBF coefficients including the two integration constants. Approximate expressions for the first-order derivative in the physical space are obtained by substituting (24) into (19)

$$\frac{du(\eta)}{d\eta} = \begin{bmatrix} H_1(\eta) & H_2(\eta) & H_3(\eta) & 1 & 0 \end{bmatrix} \mathbf{C}_1^{-1} \begin{bmatrix} \mathbf{u} \\ \frac{du_1}{d\eta} \\ \frac{du_3}{d\eta} \end{bmatrix}, \tag{25}$$

where $\eta_1 \leq \eta \leq \eta_3$ and $\mathbf{u} = [u_1, u_2, u_3]^T$. (25) can be rewritten as

$$\frac{du(\eta)}{d\eta} = \sum_{i=1}^{3} \frac{d\phi_i(\eta)}{d\eta} u_i + \frac{d\phi_4(\eta)}{d\eta} \frac{du_1}{d\eta} + \frac{d\phi_5(\eta)}{d\eta} \frac{du_3}{d\eta}, \tag{26}$$

where $\{\phi_i(\eta)\}_{i=1}^{5}$ is the set of IRBFs in the physical space. At the current time level n, (26) is taken as

$$\frac{du^n(\eta)}{d\eta} = \sum_{i=1}^{3} \frac{d\phi_i(\eta)}{d\eta} u_i^n + \frac{d\phi_4(\eta)}{d\eta} \frac{du_1^n}{d\eta} + \frac{d\phi_5(\eta)}{d\eta} \frac{du_3^n}{d\eta}, \tag{27}$$

where nodal values of the first-order derivative on the right hand side are treated as unknowns. Collocating (27) at $\eta = \eta_2$ results in

$$-\frac{d\phi_4(\eta_2)}{d\eta} \frac{du_1^n}{d\eta} + \frac{du_2^n}{d\eta} - \frac{d\phi_5(\eta_2)}{d\eta} \frac{du_3^n}{d\eta} = \frac{d\phi_1(\eta_2)}{d\eta} u_1^n + \frac{d\phi_2(\eta_2)}{d\eta} u_2^n + \frac{d\phi_3(\eta_2)}{d\eta} u_3^n, \tag{28}$$

or in the matrix-vector form

$$\begin{bmatrix} -\frac{d\phi_4(\eta_2)}{d\eta} & 1 & -\frac{d\phi_5(\eta_2)}{d\eta} \end{bmatrix} \begin{bmatrix} \frac{du_1^n}{d\eta} \\ \frac{du_2^n}{d\eta} \\ \frac{du_3^n}{d\eta} \end{bmatrix} = \begin{bmatrix} \frac{d\phi_1(\eta_2)}{d\eta} & \frac{d\phi_2(\eta_2)}{d\eta} & \frac{d\phi_3(\eta_2)}{d\eta} \end{bmatrix} \begin{bmatrix} u_1^n \\ u_2^n \\ u_3^n \end{bmatrix}. \tag{29}$$

Figure 2: Special compact 4-point 1D-IRBF stencil for boundary nodes.

At the boundary nodes, the first-order derivatives are approximated in special compact stencils. Consider the boundary node, e.g. η_1. Its associated stencil is $\{\eta_1, \eta_2, \eta_3, \eta_4\}$ as shown in Figure 2. The conversion system over this special stencil is presented as the following matrix-vector multiplication

$$
\begin{bmatrix} u_1 \\ u_2 \\ u_3 \\ u_4 \\ \frac{du_2}{d\eta} \end{bmatrix} = \underbrace{\begin{bmatrix} \overline{\mathbf{H}}_{sp} \\ \mathbf{H}_{sp} \end{bmatrix}}_{\mathbf{C}_{sp1}} \begin{bmatrix} w_1 \\ w_2 \\ w_3 \\ w_4 \\ c_1 \\ c_2 \end{bmatrix},
\tag{30}
$$

where $\mathbf{C}_{sp1}$ is the conversion matrix and $\overline{\mathbf{H}}_{sp}$, $\mathbf{H}_{sp}$ are defined as

$$
\overline{\mathbf{H}}_{sp} = \begin{bmatrix} \overline{H}_1(\eta_1) & \overline{H}_2(\eta_1) & \overline{H}_3(\eta_1) & \overline{H}_4(\eta_1) & \eta_1 & 1 \\ \overline{H}_1(\eta_2) & \overline{H}_2(\eta_2) & \overline{H}_3(\eta_2) & \overline{H}_4(\eta_2) & \eta_2 & 1 \\ \overline{H}_1(\eta_3) & \overline{H}_2(\eta_3) & \overline{H}_3(\eta_3) & \overline{H}_4(\eta_3) & \eta_3 & 1 \\ \overline{H}_1(\eta_4) & \overline{H}_2(\eta_4) & \overline{H}_3(\eta_4) & \overline{H}_4(\eta_4) & \eta_4 & 1 \end{bmatrix}.
\tag{31}
$$

$$
\mathbf{H}_{sp} = \begin{bmatrix} H_1(\eta_2) & H_2(\eta_2) & H_3(\eta_2) & H_4(\eta_2) & 1 & 0 \end{bmatrix}.
\tag{32}
$$

Solving (30) yields

$$
\begin{bmatrix} w_1 \\ w_2 \\ w_3 \\ w_4 \\ c_1 \\ c_2 \end{bmatrix} = \mathbf{C}_{sp1}^{-1} \begin{bmatrix} u_1 \\ u_2 \\ u_3 \\ u_4 \\ \frac{du_2}{d\eta} \end{bmatrix}.
\tag{33}
$$

The boundary value of the first-order derivative of u is thus obtained by substituting (33) into (19) and taking $\eta = \eta_1$

$$
\frac{du(\eta_1)}{d\eta} = \begin{bmatrix} H_1(\eta_1) & H_2(\eta_1) & H_3(\eta_1) & H_4(\eta_1) & 1 & 0 \end{bmatrix} \mathbf{C}_{sp1}^{-1} \begin{bmatrix} \mathbf{u} \\ \frac{du_2}{d\eta} \end{bmatrix},
\tag{34}
$$

where $\mathbf{u} = [u_1, u_2, u_3, u_4]^T$. (34) can be rewritten as

$$\frac{du(\eta_1)}{d\eta} = \sum_{i=1}^{4} \frac{d\phi_{spi}(\eta_1)}{d\eta} u_i + \frac{d\phi_{sp5}(\eta_1)}{d\eta} \frac{du_2}{d\eta}. \tag{35}$$

At the current time level n, (35) is taken as

$$\frac{du^n(\eta_1)}{d\eta} = \sum_{i=1}^{4} \frac{d\phi_{spi}(\eta_1)}{d\eta} u_i^n + \frac{d\phi_{sp5}(\eta_1)}{d\eta} \frac{du_2^n}{d\eta}, \tag{36}$$

or

$$\frac{du_1^n}{d\eta} - \frac{d\phi_{sp5}(\eta_1)}{d\eta} \frac{du_2^n}{d\eta} = \frac{d\phi_{sp1}(\eta_1)}{d\eta} u_1^n + \frac{d\phi_{sp2}(\eta_1)}{d\eta} u_2^n + \frac{d\phi_{sp3}(\eta_1)}{d\eta} u_3^n + \frac{d\phi_{sp4}(\eta_1)}{d\eta} u_4^n, \tag{37}$$

or in the matrix-vector form

$$\begin{bmatrix} 1 & -\frac{d\phi_{sp5}(\eta_1)}{d\eta} & 0 & 0 \end{bmatrix} \begin{bmatrix} \frac{du_1^n}{d\eta} \\ \frac{du_2^n}{d\eta} \\ \frac{du_3^n}{d\eta} \\ \frac{du_4^n}{d\eta} \end{bmatrix} = \begin{bmatrix} \frac{d\phi_{sp1}(\eta_1)}{d\eta} & \frac{d\phi_{sp2}(\eta_1)}{d\eta} & \frac{d\phi_{sp3}(\eta_1)}{d\eta} & \frac{d\phi_{sp4}(\eta_1)}{d\eta} \end{bmatrix} \begin{bmatrix} u_1^n \\ u_2^n \\ u_3^n \\ u_4^n \end{bmatrix}. \tag{38}$$

In a similar manner, one is able to calculate the first-order derivative of u at the boundary node η_{n_η}. The IRBF system on a grid line for the first-order derivative of u is obtained by letting the interior node taking values from 2 to $(n_\eta - 1)$ in (29) and making use of (38) for the boundary nodes 1 and n_η, resulting in

$$\mathbf{Q}_\eta \mathbf{u}_\eta^n = \mathbf{R}_\eta \mathbf{u}^n, \tag{39}$$

where $\mathbf{Q}_\eta$ and $\mathbf{R}_\eta$ are $n_\eta \times n_\eta$ matrices.

4.2 Second-order derivative compact approximations

Extra information used in the compact approximation of the second-order derivative are chosen as $\frac{d^2 u_1}{d\eta^2}$ and $\frac{d^2 u_3}{d\eta^2}$. We construct the conversion system over a 3-point stencil associated with an interior node in the form

$$\begin{bmatrix} u_1 \\ u_2 \\ u_3 \\ \frac{d^2 u_1}{d\eta^2} \\ \frac{d^2 u_3}{d\eta^2} \end{bmatrix} = \underbrace{\begin{bmatrix} \overline{\mathbf{H}} \\ \mathbf{G} \end{bmatrix}}_{\mathbf{C}_2} \begin{bmatrix} w_1 \\ w_2 \\ w_3 \\ c_1 \\ c_2 \end{bmatrix}, \tag{40}$$

where $\frac{d^2 u_i}{d\eta^2} = \frac{d^2 u}{d\eta^2}(\eta_i)$ with $i \in \{1,2,3\}$; $\mathbf{C}_2$ is the conversion matrix; $\overline{\mathbf{H}}$ is defined as before (i.e. (22)) and $\mathbf{G}$ is defined as

$$\mathbf{G} = \begin{bmatrix} G_1(\eta_1) & G_2(\eta_1) & G_3(\eta_1) & 0 & 0 \\ G_1(\eta_3) & G_2(\eta_3) & G_3(\eta_3) & 0 & 0 \end{bmatrix}. \tag{41}$$

Solving (40) yields

$$\begin{bmatrix} w_1 \\ w_2 \\ w_3 \\ c_1 \\ c_2 \end{bmatrix} = \mathbf{C}_2^{-1} \begin{bmatrix} u_1 \\ u_2 \\ u_3 \\ \frac{d^2 u_1}{d\eta^2} \\ \frac{d^2 u_3}{d\eta^2} \end{bmatrix}, \tag{42}$$

which maps the vector of nodal values of the function and its second-order derivative to the vector of RBF coefficients including the two integration constants. Approximate expressions for the second-order derivative in the physical space are obtained by substituting (42) into (18)

$$\frac{d^2 u(\eta)}{d\eta^2} = \begin{bmatrix} G_1(\eta) & G_2(\eta) & G_3(\eta) & 0 & 0 \end{bmatrix} \mathbf{C}_2^{-1} \begin{bmatrix} \mathbf{u} \\ \frac{d^2 u_1}{d\eta^2} \\ \frac{d^2 u_3}{d\eta^2} \end{bmatrix}, \tag{43}$$

where $\eta_1 \leq \eta \leq \eta_3$ and $\mathbf{u} = [u_1, u_2, u_3]^T$. (43) can be rewritten as

$$\frac{d^2 u(\eta)}{d\eta^2} = \sum_{i=1}^{3} \frac{d^2 \phi_i(\eta)}{d\eta^2} u_i + \frac{d^2 \phi_4(\eta)}{d\eta^2} \frac{d^2 u_1}{d\eta^2} + \frac{d^2 \phi_5(\eta)}{d\eta^2} \frac{d^2 u_3}{d\eta^2}. \tag{44}$$

At the current time level n

$$\frac{d^2 u^n(\eta)}{d\eta^2} = \sum_{i=1}^{3} \frac{d^2 \phi_i(\eta)}{d\eta^2} u_i^n + \frac{d^2 \phi_4(\eta)}{d\eta^2} \frac{d^2 u_1^n}{d\eta^2} + \frac{d^2 \phi_5(\eta)}{d\eta^2} \frac{d^2 u_3^n}{d\eta^2}, \tag{45}$$

where nodal values of the second-order derivative on the right hand side are treated as unknowns. Collocating (45) at $\eta = \eta_2$ leads to

$$-\frac{d^2 \phi_4(\eta_2)}{d\eta^2} \frac{d^2 u_1^n}{d\eta^2} + \frac{d^2 u_2^n}{d\eta^2} - \frac{d^2 \phi_5(\eta_2)}{d\eta^2} \frac{d^2 u_3^n}{d\eta^2} = \frac{d^2 \phi_1(\eta_2)}{d\eta^2} u_1^n + \frac{d^2 \phi_2(\eta_2)}{d\eta^2} u_2^n + \frac{d^2 \phi_3(\eta_2)}{d\eta^2} u_3^n, \tag{46}$$

or in the matrix-vector form

$$\begin{bmatrix} -\frac{d^2\phi_4(\eta_2)}{d\eta^2} & 1 & -\frac{d^2\phi_5(\eta_2)}{d\eta^2} \end{bmatrix} \begin{bmatrix} \frac{d^2u_1^n}{d\eta^2} \\ \frac{d^2u_2^n}{d\eta^2} \\ \frac{d^2u_3^n}{d\eta^2} \end{bmatrix} = \begin{bmatrix} \frac{d^2\phi_1(\eta_2)}{d\eta^2} & \frac{d^2\phi_2(\eta_2)}{d\eta^2} & \frac{d^2\phi_3(\eta_2)}{d\eta^2} \end{bmatrix} \begin{bmatrix} u_1^n \\ u_2^n \\ u_3^n \end{bmatrix}. \tag{47}$$

At the boundary nodes, the second-order derivatives are approximated in special compact stencils. Consider the boundary node, e.g. η_1. Its associated stencil is $\{\eta_1, \eta_2, \eta_3, \eta_4\}$ as shown in Figure 2. The conversion system over this special stencil is presented as the following matrix-vector multiplication

$$\begin{bmatrix} u_1 \\ u_2 \\ u_3 \\ u_4 \\ \frac{d^2u_2}{d\eta} \end{bmatrix} = \underbrace{\begin{bmatrix} \overline{\mathbf{H}}_{sp} \\ \mathbf{G}_{sp} \end{bmatrix}}_{\mathbf{C}_{sp2}} \begin{bmatrix} w_1 \\ w_2 \\ w_3 \\ w_4 \\ c_1 \\ c_2 \end{bmatrix}, \tag{48}$$

where $\mathbf{C}_{sp2}$ is the conversion matrix; $\overline{\mathbf{H}}_{sp}$ is defined as before (i.e. (31)) and $\mathbf{G}_{sp}$ is defined as

$$\mathbf{G}_{sp} = \begin{bmatrix} G_1(\eta_2) & G_2(\eta_2) & G_3(\eta_2) & G_4(\eta_2) & 0 & 0 \end{bmatrix}. \tag{49}$$

Solving (48) yields

$$\begin{bmatrix} w_1 \\ w_2 \\ w_3 \\ w_4 \\ c_1 \\ c_2 \end{bmatrix} = \mathbf{C}_{sp2}^{-1} \begin{bmatrix} u_1 \\ u_2 \\ u_3 \\ u_4 \\ \frac{d^2u_2}{d\eta^2} \end{bmatrix}. \tag{50}$$

The boundary value of the second-order derivative of u is thus obtained by substituting (50) into (18) and taking $\eta = \eta_1$

$$\frac{d^2u(\eta_1)}{d\eta^2} = \begin{bmatrix} G_1(\eta_1) & G_2(\eta_1) & G_3(\eta_1) & G_4(\eta_1) & 0 & 0 \end{bmatrix} \mathbf{C}_{sp2}^{-1} \begin{bmatrix} \mathbf{u} \\ \frac{d^2u_2}{d\eta^2} \end{bmatrix}, \tag{51}$$

where $\mathbf{u} = [u_1, u_2, u_3, u_4]^T$. (51) can be rewritten as

$$\frac{d^2u(\eta_1)}{d\eta^2} = \sum_{i=1}^{4} \frac{d^2\phi_{spi}(\eta_1)}{d\eta^2} u_i + \frac{d^2\phi_{sp5}(\eta_1)}{d\eta^2} \frac{d^2u_2}{d\eta^2}. \tag{52}$$

At the current time level n, (52) is taken as

$$\frac{d^2 u^n(\eta_1)}{d\eta^2} = \sum_{i=1}^{4} \frac{d^2 \phi_{spi}(\eta_1)}{d\eta^2} u_i^n + \frac{d^2 \phi_{sp5}(\eta_1)}{d\eta^2} \frac{d^2 u_2^n}{d\eta^2}, \tag{53}$$

or

$$\frac{d^2 u_1^n}{d\eta^2} - \frac{d^2 \phi_{sp5}(\eta_1)}{d\eta^2} \frac{d^2 u_2^n}{d\eta^2} = \frac{d^2 \phi_{sp1}(\eta_1)}{d\eta^2} u_1^n + \frac{d^2 \phi_{sp2}(\eta_1)}{d\eta^2} u_2^n$$
$$+ \frac{d^2 \phi_{sp3}(\eta_1)}{d\eta^2} u_3^n + \frac{d^2 \phi_{sp4}(\eta_1)}{d\eta^2} u_4^n, \tag{54}$$

or in the matrix-vector form

$$\begin{bmatrix} 1 & -\frac{d^2 \phi_{sp5}(\eta_1)}{d\eta^2} & 0 & 0 \end{bmatrix} \begin{bmatrix} \frac{d^2 u_1^n}{d\eta^2} \\ \frac{d^2 u_2^n}{d\eta^2} \\ \frac{d^2 u_3^n}{d\eta^2} \\ \frac{d^2 u_4^n}{d\eta^2} \end{bmatrix} = \begin{bmatrix} \frac{d^2 \phi_{sp1}(\eta_1)}{d\eta^2} & \frac{d^2 \phi_{sp2}(\eta_1)}{d\eta^2} & \frac{d^2 \phi_{sp3}(\eta_1)}{d\eta^2} & \frac{d^2 \phi_{sp4}(\eta_1)}{d\eta^2} \end{bmatrix} \begin{bmatrix} u_1^n \\ u_2^n \\ u_3^n \\ u_4^n \end{bmatrix}.$$
$$\tag{55}$$

In a similar manner, one is able to calculate the second-order derivative of u at the boundary node η_{n_η}. The IRBF system on a grid line for the second-order derivative of u is obtained by letting the interior node taking values from 2 to $(n_\eta - 1)$ in (47) and making use of (55) for the boundary nodes 1 and n_η, resulting in

$$\mathbf{Q}_{\eta\eta}\mathbf{u}_{\eta\eta}^n = \mathbf{R}_{\eta\eta}\mathbf{u}^n, \tag{56}$$

where $\mathbf{Q}_{\eta\eta}$ and $\mathbf{R}_{\eta\eta}$ are $n_\eta \times n_\eta$ matrices. It is noted that, for brevity, we use the same notations to represent the set of IRBFs and the RBF coefficients for the approximation of first- and second-order derivatives. In fact, for example, the basis functions $\{\phi_i(\eta)\}_{i=1}^5$ in (26) are different from those in (44); and, the coefficient set $[w_1, w_2, w_3, w_4, c_1, c_2]^T$ in (30) is not the same as that in (48).

5 Numerical examples

We chose the multiquadric (MQ) function as the basis function in the present calculations

$$G_i(x) = \sqrt{(x - c_i)^2 + a_i^2}, \tag{57}$$

where c_i and a_i are the centre and the width of the i-th MQ, respectively. For each stencil, the set of nodal points is taken to be the same as the set of MQ centres.

We simply choose the MQ width as $a_i = \beta h_i$, where β is a positive scalar and h_i is the distance between the i-th node and its closest neighbour. The value of $\beta = 40$ is chosen for calculation in Section 5.4 and $\beta = 50$ for the rest of calculations in the present work. We evaluate the performance of the present scheme through the following measures

i. the root mean square error (RMS) is defined as

$$RMS = \sqrt{\frac{\sum_{i=1}^{N} \left(f_i - \overline{f}_i\right)^2}{N}}, \tag{58}$$

where f_i and $\overline{f}_i$ are the computed and exact values of the solution f at the i-th node, respectively; and, N is the number of nodes over the whole domain.

ii. the maximum absolute error (L_∞) is defined as

$$L_\infty = \max_{i=1,\dots,N} \left|f_i - \overline{f}_i\right|. \tag{59}$$

iii. the global convergence rate with respect to the grid refinement is defined through

$$RMS(h) \approx \gamma h^\alpha = O(h^\alpha), \tag{60}$$

where h is the grid size; and, γ and α are exponential model's parameters.

iv. a flow is considered as reaching its steady state when

$$\sqrt{\frac{\sum_{i=1}^{N} \left(f_i^n - f_i^{n-1}\right)^2}{N}} < 10^{-9}. \tag{61}$$

5.1 *Poisson equation in rectangular domain*

In order to study the spatial accuracy of the present CIRBF approximation scheme in a rectangular domain, we consider the following Poisson equation [Mai-Duy and Tran-Cong (2010)]

$$\frac{d^2u}{dx_1^2} + \frac{d^2u}{dx_2^2}$$
$$= 4(1 - \pi^2)\{\sin(\pi(2x_1-1))\sinh(2x_2-1) + 4\cosh(2(2x_1-1))\cos(2\pi(2x_2-1))\}, \tag{62}$$

subject to Dirichlet boundary condition derived from the following exact solution

$$\bar{u} = \sin(\pi(2x_1 - 1))\sinh(2x_2 - 1) + \cosh(2(2x_1 - 1))\cos(2\pi(2x_2 - 1)), \qquad (63)$$

on a square domain $[0, 1]^2$. The calculations are carried out on a set of uniform grids of $\{41 \times 41, 51 \times 51, ..., 91 \times 91\}$. Figure 3 shows that present scheme outperforms the fourth-order compact FDM (Finite Difference Method) by Tian, Liang, and Yu (2011) and second-order standard FDM in terms of both accuracy and rates of convergence. The solutions converge as $O(h^{5.23})$ for the present scheme, $O(h^{4.56})$ for the compact FDM, and $O(h^{1.99})$ for the standard FDM. Figure 4 shows that the matrix condition number grows with approximately the same rate of $O(h^{-2.00})$ for the three methods.
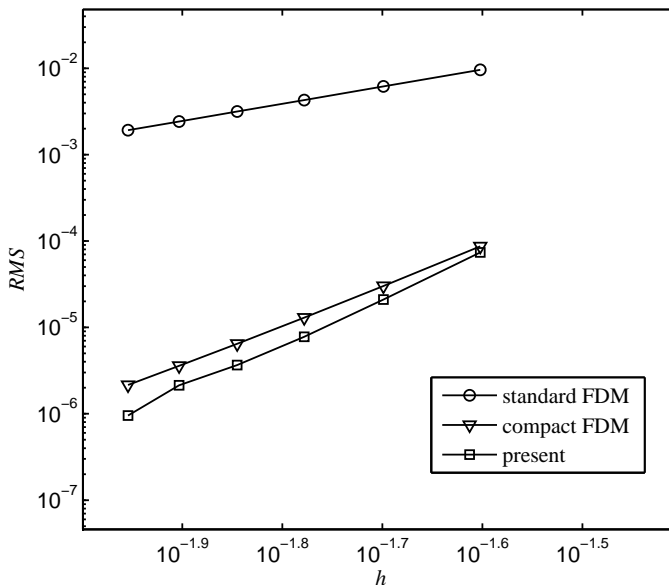

Figure 3: Poisson equation, rectangular domain, $\{41 \times 41, 51 \times 51, ..., 91 \times 91\}$: The effect of grid size h on the solution accuracy *RMS*.

5.2   *Poisson equation in non-rectangular domain*

To study the spatial accuracy of the present CIRBF approximation scheme in a non-rectangular domain, we consider the following Poisson equation [Mai-Duy
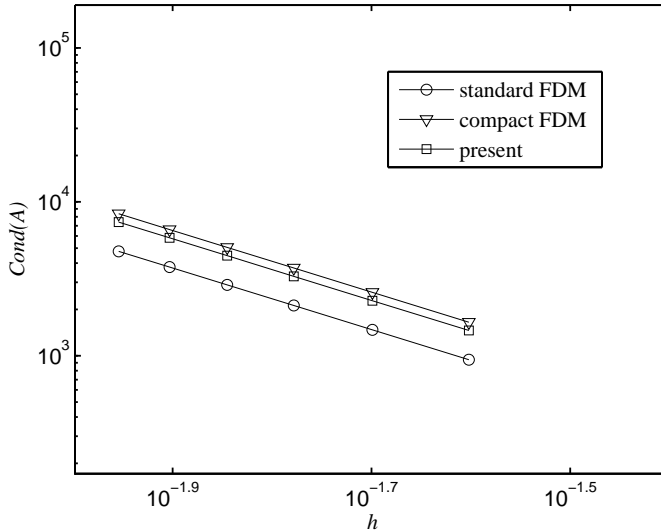
Figure 4: Poisson equation, rectangular domain, $\{41 \times 41, 51 \times 51, ..., 91 \times 91\}$: The effect of grid size h on the matrix condition number.

and Tran-Cong (2010)]

$$\frac{d^2u}{dx_1^2} + \frac{d^2u}{dx_2^2} = 4(1 - \pi^2) \left\{ \sin(2\pi x_1) \sinh(2x_2) + 4\cosh(4x_1) \cos(4\pi x_2) \right\}, \qquad (64)$$

subject to Dirichlet boundary condition derived from the following exact solution

$$\bar{u} = \sin(2\pi x_1) \sinh(2x_2) + \cosh(4x_1) \cos(4\pi x_2), \qquad (65)$$

on a circular domain with radius of 1/2. The problem domain is embedded in a uniform Cartesian grid and the grid nodes exterior to the domain are removed. The interior nodes falling within a small distance $\delta = h/8$, where h is the grid size, to the boundary will also be discarded [Mai-Duy and Tran-Cong (2010)]. The boundary nodes are generated through the intersection of the grid lines and the boundary as demonstrated in Figure 5. Calculations are carried out on a set of uniform grids, $\{20 \times 20, 30 \times 30, ..., 90 \times 90\}$. Figure 6 shows that the present compact IRBF has better performance than second- and fourth-order compact FDM schemes proposed by Gamet, Ducros, Nicoud, and Poinsot (1999). The present scheme yields a fast rate of convergence of $O(h^{4.38})$ while the compact FDM produces a rate of $O(h^{3.99})$ for the fourth-order scheme and $O(h^{1.99})$ for the second-order scheme. Figure 7 shows that the matrix condition number increases with approximately the same rate of $O(h^{-1.99})$ for the three methods.
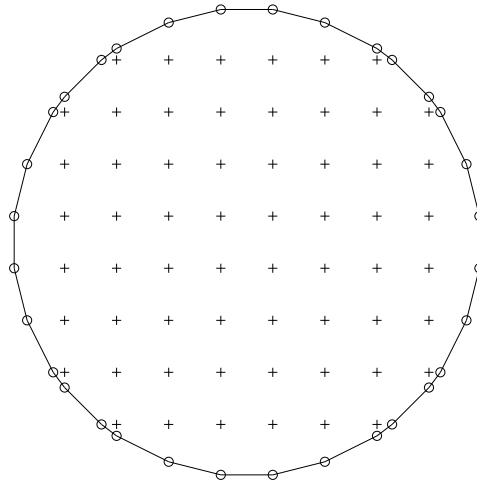
Figure 5: Poisson equation, non-rectangular domain, spatial discretisation: +, interior nodes; ○, boundary nodes.
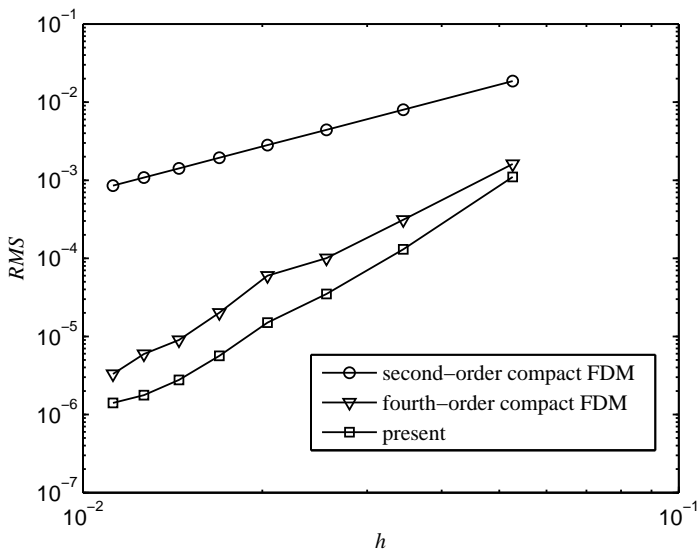

Figure 6: Poisson equation, non-rectangular domain, $\{20 \times 20, 30 \times 30, ..., 90 \times 90\}$: The effect of grid size h on the solution accuracy RMS.
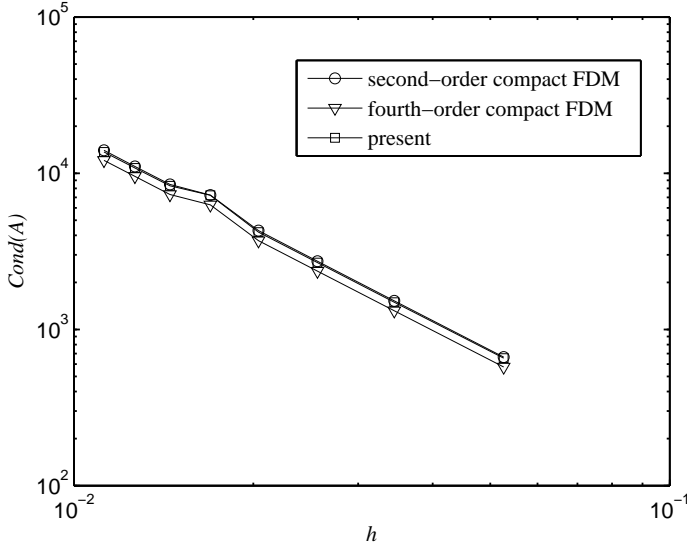
Figure 7: Poisson equation, non-rectangular domain, $\{20 \times 20, 30 \times 30, ..., 90 \times 90\}$: The effect of grid size h on the matrix condition number.

5.3 Taylor-Green vortex in rectangular domain

To study the performance of the fully coupled approach, based on CIRBF approximation, in simulating viscous flow in a rectangular domain, we consider a transient flow problem, namely Taylor-Green vortex [Tian, Liang, and Yu (2011)]. This problem is governed by the Navier-Stokes equations (4)-(6) and has the analytical solutions

$$\bar{u}(x_1, x_2, t) = -\cos(kx_1)\sin(kx_2)\exp(-2k^2 t/Re), \tag{66}$$

$$\bar{v}(x_1, x_2, t) = \sin(kx_1)\cos(kx_2)\exp(-2k^2 t/Re), \tag{67}$$

$$\bar{p}(x_1, x_2, t) = -1/4\{\cos(2kx_1) + \cos(2kx_2)\}\exp(-4k^2 t/Re), \tag{68}$$

where $0 \le x_1, x_2 \le 2\pi$. Calculations are carried out for $k = 2$ on a set of uniform grid, $\{11 \times 11, 21 \times 21, ..., 51 \times 51\}$. A fixed time step $\Delta t = 0.002$ and $Re = 100$ are employed. Numerical solutions are computed at $t = 2$. The exact solution, i.e. equations (66)-(68), provides the initial field at $t = 0$ and the time-dependent boundary conditions. Table 1 shows the accuracy comparison between the present scheme and compact FDM scheme of Tian, Liang, and Yu (2011) in terms of *RMS* errors and convergence rates. It is seen that the present scheme produces better accuracy

and better convergence rates than the scheme of Tian, Liang, and Yu (2011), i.e. $O(h^{5.35})$ compared to $O(h^{2.92})$ for the velocity and $O(h^{4.48})$ compared to $O(h^{3.28})$ for the pressure.

5.4   *Taylor-Green vortex in non-rectangular domain*

In order to analyse the performance of the combination of the fully coupled approach and CIRBF approximation scheme in solving the transient viscous flow in a non-rectangular domain, we consider the case of an array of decaying vortices with the analytical solutions [Uhlmann (2005)] described by

$$\bar{u}(x_1, x_2, t) = \sin(\pi x_1)\cos(\pi x_2)\exp(-2\pi^2 t/Re), \tag{69}$$

$$\bar{v}(x_1, x_2, t) = -\sin(\pi x_2)\cos(\pi x_1)\exp(-2\pi^2 t/Re), \tag{70}$$

$$\bar{p}(x_1, x_2, t) = 1/2\left\{\cos^2(\pi x_2) - \sin^2(\pi x_1)\right\}\exp(-4\pi^2 t/Re). \tag{71}$$

The flow is computed in an embedded circular domain with radius of unity and centred at the origin of the computational domain $\Omega = [-1.5, 1.5] \times [-1.5, 1.5]$. The interior nodes are chosen and the boundary nodes are generated in a similar manner described in Section 5.2. Calculations are carried out on a set of uniform grids, $\{10 \times 10, 20 \times 20, ..., 50 \times 50\}$. The Reynolds number is set to be $Re = 5$ and numerical solutions are computed at $t = 0.3$ using a fixed time step $\Delta t = 0.001$. The initial field at $t = 0$ and the time-dependent boundary conditions are given by (69)-(71). Table 2 illustrates the accuracy comparison between the present scheme and FDM approach of Uhlmann (2005) in terms of maximum errors and convergence rates. It is observed that present scheme produces lower errors with better convergence rates, i.e. $O(h^{4.44})$ for the u-velocity and $O(h^{4.59})$ for the v-velocity in comparison with $O(h^{2.13})$ for both u- and v-velocities given by the approach of Uhlmann (2005).

5.5   *Lid driven cavity flow*

The classical lid driven cavity flow has been considered as a test problem for the evaluation of numerical methods and the validation of fluid flow solvers for the past decades. Figure 8 shows the problem definition and boundary conditions. Uniform grids of $\{31 \times 31, 51 \times 51, 71 \times 71, 91 \times 91, 111 \times 111, 129 \times 129\}$ and a range of $Re \in \{100, 400, 1000, 3200\}$ are employed in the simulation. A fixed time step is chosen to be $\Delta t = 0.001$. Results of the present scheme are compared with those of some others [Ghia, Ghia, and Shin (1982); Gresho, Chan, Lee, and Upson (1984); Bruneau and Jouron (1990); Deng, Piquet, Queutey, and Visonneau (1994b); Botella and Peyret (1998); Sahin and Owens (2003); Thai-Quang, Le-Cao, Mai-Duy, and Tran-Cong (2012)]. From the literature, FDM results using

Table 1: Taylor-Green Vortex, rectangular domain: *RMS* errors and convergence rates.

Grid	present			compact FDM [Tian et al. (2011)]		
	u-error	*v*-error	*p*-error	*u*-error	*v*-error	*p*-error
11×11	1.7797233E-01	1.7797723E-01	3.0668704E-01	7.0070489E-02	7.0070489E-02	1.0764149E-01
21×21	4.6366355E-03	4.6366340E-03	8.5913505E-03	9.0692193E-03	9.0692193E-03	1.0567607E-02
31×31	5.3168859E-04	5.3168061E-04	2.6550518E-03	2.8851487E-03	2.8851487E-03	2.9103288E-03
41×41	1.0970214E-04	1.0968156E-04	3.4713723E-04	1.2238736E-03	1.2238736E-03	1.1356134E-03
51×51	3.2428099E-05	3.2378594E-05	2.6244035E-04	6.3063026E-04	6.3063026E-04	5.3933641E-04
Rate	$O(h^{5.35})$	$O(h^{5.35})$	$O(h^{4.48})$	$O(h^{2.92})$	$O(h^{2.92})$	$O(h^{3.28})$

Table 2: Taylor Green Vortex, non-rectangular domain: Maximum errors (L_∞) and convergence rates.

| Grid	present			FDM [Uhlmann et al. (2005)]		
	u-error	v-error	p-error	u-error	v-error	p-error
10×10	5.0940713E-02	3.9890094E-02	9.5986185E-02	–	–	–
20×20	1.1003665E-03	7.9266552E-04	2.2013746E-03	–	–	–
30×30	9.7670238E-05	8.1362620E-05	5.1711179E-04	$\approx$1.056E-02	$\approx$1.056E-02	–
40×40	5.8426984E-05	2.8665169E-05	2.1616129E-04	$\approx$5.520E-03	$\approx$5.520E-03	–
50×50	3.3759336E-05	2.3569385E-05	1.4680716E-04	$\approx$3.441E-03	$\approx$3.441E-03	–
Rate	$O(h^{4.44})$	$O(h^{4.59})$	$O(h^{3.88})$	$\approx O(h^{2.13})$	$\approx O(h^{2.13})$	–
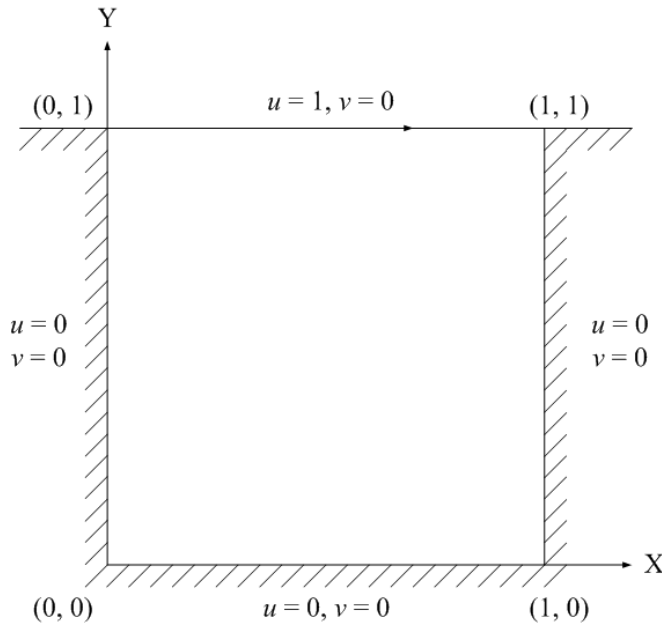
Figure 8: Lid driven cavity: problem configuration and boundary conditions.

very dense grids presented by Ghia, Ghia, and Shin (1982) and pseudo-spectral results presented by Botella and Peyret (1998) have been referred to as "Benchmark" results for comparison purposes.

Tables 3, 4, 5, and 6 show the present results for the extrema of the vertical and horizontal velocity profiles along the horizontal and vertical centrelines of the cavity for several Reynolds numbers. For $Re = 100$ (Table 3) and $Re = 1000$ (Table 4), the "Errors" are evaluated relative to "Benchmark" results of Botella and Peyret (1998). The results obtained by the present scheme are very comparable with others.

Figure 9 displays velocity profiles along the vertical and horizontal centrelines for different grid sizes at $Re = 1000$, where a grid convergence of the present scheme is obviously observed (i.e. the present solution approaches the benchmark solution with a fast rate as the grid density is increased). The present scheme effectively achieves the benchmark results with a grid of only 91×91 in comparison with the grid of 129×129 used to obtain the benchmark results in [Ghia, Ghia, and Shin (1982)]. In addition, those velocity profiles at $Re \in \{100, 400, 1000, 3200\}$ with the grid size of $\{51 \times 51, 71 \times 71, 91 \times 91, 129 \times 129\}$, respectively, are displayed in Figure 10, where the present solutions match the benchmark ones very well.

Table 3: Lid driven cavity, $Re = 100$: Extrema of the vertical and horizontal velocity profiles along the horizontal and vertical centrelines of the cavity, respectively. "Errors" are relative to the "Benchmark" data.

Method	Grid	u_{min}	Error (%)	y_{min}	v_{max}	Error (%)	x_{max}	v_{min}	Error (%)	x_{min}
Present	31×31	-0.2132676	0.36	0.4586	0.1788936	0.38	0.2374	-0.2527995	0.40	0.8101
Present	51×51	-0.2139898	0.02	0.4581	0.1795821	0.01	0.2371	-0.2538354	0.01	0.8104
Present	71×71	-0.2140390	0.00	0.4581	0.1795960	0.01	0.2370	-0.2538423	0.02	0.8104
CIRBF (u, v, p), [Thai-Quang (2012b)]	31×31	-0.2102259	1.78	0.4578	0.1768808	1.50	0.2370	-0.2501843	1.43	0.8107
CIRBF (u, v, p), [Thai-Quang (2012b)]	51×51	-0.2121503	0.88	0.4579	0.1781849	0.77	0.2372	-0.2520400	0.69	0.8107
FVM (u, v, p), [Deng (1994b)]	64×64	-0.21315	0.42	—	0.17896	0.34	—	-0.25339	0.16	—
FDM $(\psi - \omega)$, [Ghia (1982)]	129×129	-0.21090	1.47	0.4531	0.17527	2.40	0.2344	-0.24533	3.34	0.8047
FDM (u, v, p), [Bruneau (1990)]	129×129	-0.2106	1.61	0.4531	0.1786	0.54	0.2344	-0.2521	0.67	0.8125
FVM (u, v, p), [Sahin (2003)]	257×257	-0.213924	0.06	0.4598	0.180888	0.73	0.2354	-0.256603	1.10	0.8127
Benchmark, [Botella (1998)]		-0.2140424		0.4581	0.1795728		0.2370	-0.2538030		0.8104

Table 4: Lid driven cavity, $Re = 1000$: Extrema of the vertical and horizontal velocity profiles along the horizontal and vertical centrelines of the cavity, respectively. "Errors" are relative to the "Benchmark" data.

Method	Grid	u_{min}	Error (%)	y_{min}	v_{max}	Error (%)	x_{max}	v_{min}	Error (%)	x_{min}
Present	51×51	-0.3611357	7.06	0.1819	0.3481667	7.63	0.1621	-0.4853383	7.92	0.9025
Present	71×71	-0.3807425	2.01	0.1741	0.3685353	2.23	0.1593	-0.5156774	2.16	0.9079
Present	91×91	-0.3857664	0.72	0.1725	0.3738367	0.82	0.1585	-0.5231499	0.75	0.9089
Present	111×111	-0.3873278	0.32	0.1720	0.3755235	0.38	0.1582	-0.5254043	0.32	0.9091
CIRBF (u, v, p), [Thai-Quang (2012b)]	71×71	-0.3755225	3.36	0.1753	0.3637009	3.51	0.1608	-0.5086961	3.49	0.9078
CIRBF (u, v, p), [Thai-Quang (2012b)]	91×91	-0.3815923	1.80	0.1735	0.3698053	1.89	0.1594	-0.5174658	1.82	0.9085
CIRBF (u, v, p), [Thai-Quang (2012b)]	111×111	-0.3840354	1.17	0.1728	0.3722634	1.24	0.1588	-0.5209683	1.16	0.9088
CIRBF (u, v, p), [Thai-Quang (2012b)]	129×129	-0.3848064	0.97	0.1724	0.3729119	1.07	0.1586	-0.5223350	0.90	0.9089
FVM (u, v, p), [Deng (1994b)]	128×128	-0.38511	0.89	—	0.37369	0.86	—	-0.5228	0.81	—
FDM $(\psi - \omega)$, [Ghia (1982)]	129×129	-0.38289	1.46	0.1719	0.37095	1.59	0.1563	-0.5155	2.20	0.9063
FEM (u, v, p), [Gresho (1984)]	129×129	-0.375	3.49	0.160	0.362	3.96	0.160	-0.516	2.10	0.906
FDM (u, v, p), [Bruneau (1990)]	256×256	-0.3764	3.13	0.1602	0.3665	2.77	0.1523	-0.5208	1.19	0.9102
FVM (u, v, p), [Sahin (2003)]	257×257	-0.388103	0.12	0.1727	0.376910	0.01	0.1573	-0.528447	0.26	0.9087
Benchmark, [Botella (1998)]		-0.3885698		0.1717	0.3769447		0.1578	-0.5270771		0.9092

Table 5: Lid driven cavity, $Re = 400$: Extrema of the vertical and horizontal velocity profiles along the horizontal and vertical centrelines of the cavity, respectively.

Method	Grid	u_{min}	y_{min}	v_{max}	x_{max}	v_{min}	x_{min}
Present	51×51	-0.325864	0.2809	0.300815	0.2265	-0.450157	0.8619
Present	71×71	-0.328095	0.2801	0.303156	0.2257	-0.453380	0.8622
Present	91×91	-0.328548	0.2800	0.303655	0.2254	-0.453936	0.8623
CIRBF (u, v, p), [Thai-Quang (2012b)]	51×51	-0.323158	0.2814	0.297493	0.2248	-0.442770	0.8605
CIRBF (u, v, p), [Thai-Quang (2012b)]	71×71	-0.325168	0.2804	0.300818	0.2252	-0.449146	0.8620
FVM (u, v, p), [Deng (1994b)]	128×128	-0.32751	—	0.30271	—	-0.45274	—
FDM $(\psi - \omega)$, [Ghia (1982)]	129×129	-0.327726	0.2813	0.30203	0.2266	-0.44993	0.8594
FVM (u, v, p), [Sahin (2003)]	257×257	-0.328375	0.2815	0.304447	0.2253	-0.456316	0.8621

Table 6: Lid driven cavity, $Re = 3200$: Extrema of the vertical and horizontal velocity profiles along the horizontal and vertical centrelines of the cavity, respectively.

Method	Grid	u_{min}	y_{min}	v_{max}	x_{max}	v_{min}	x_{min}
Present	91×91	-0.390803	0.1042	0.390298	0.1001	-0.503019	0.9394
Present	111×111	-0.411768	0.0983	0.409752	0.0985	-0.533705	0.9438
Present	129×129	-0.421587	0.0960	0.419126	0.0979	-0.547987	0.9455
FEM (u, v, p), [Gresho (1984)]	129×129	-0.420	0.084	0.415	0.094	-0.560	0.945
FDM $(\psi - \omega)$, [Ghia (1982)]	129×129	-0.41933	0.1016	0.42768	0.0938	-0.54053	0.9453
FVM (u, v, p), [Sahin (2003)]	257×257	-0.435402	0.0921	0.432448	0.0972	-0.569145	0.9491
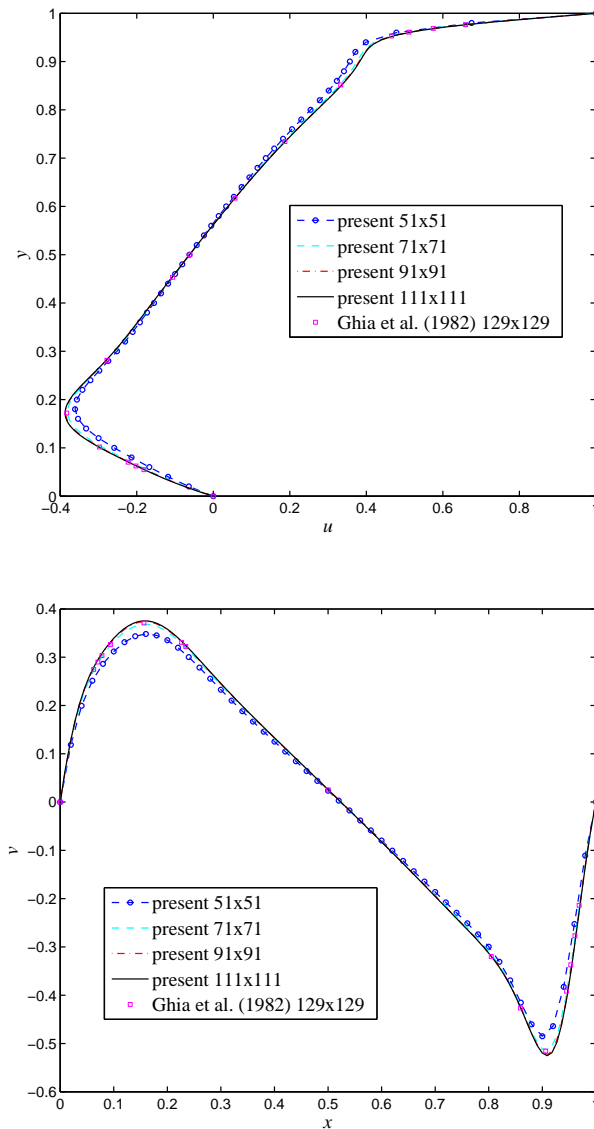
Figure 9: Lid driven cavity, $Re = 1000$: Profiles of the u-velocity along the vertical centreline and the v-velocity along the horizontal centreline as grid density increases. It is noted that the curves for the last two grids are indistinguishable and in good agreement with the benchmark results of [Ghia, Ghia, and Shin (1982)].
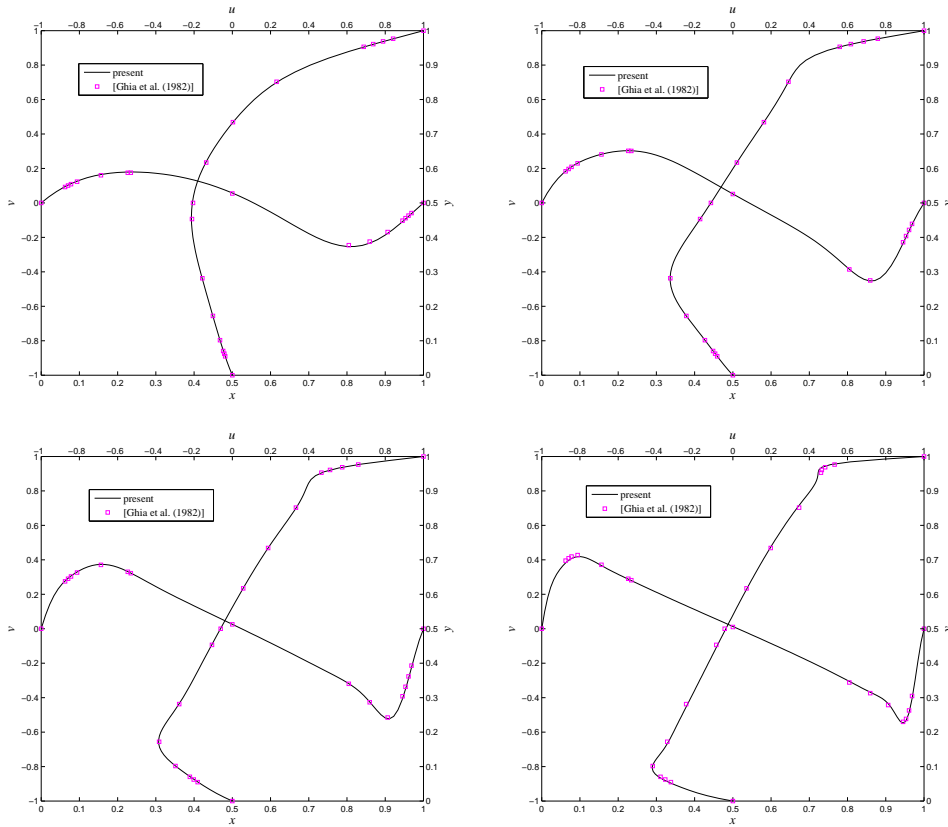
Figure 10: Lid driven cavity: Profiles of the *u*-velocity along the vertical centreline and the *v*-velocity along the horizontal centreline for $Re = 100$ (top-left), $Re = 400$ (top-right), $Re = 1000$ (bottom-left), and $Re = 3200$ (bottom-right) with the grid of 51×51, 71×71, 91×91, and 129×129, respectively.

To exhibit contour plots of the flow, a range of $Re \in \{100, 400, 1000, 3200\}$ and the grid of $\{51 \times 51, 71 \times 71, 91 \times 91, 129 \times 129\}$ are employed, respectively. Figures 11 and 12 show streamlines and iso-vorticity lines, which are derived from the velocity field. Figure 13 shows the pressure deviation contours of the present simulations. These plots are also in good agreement with those reported in the literature.
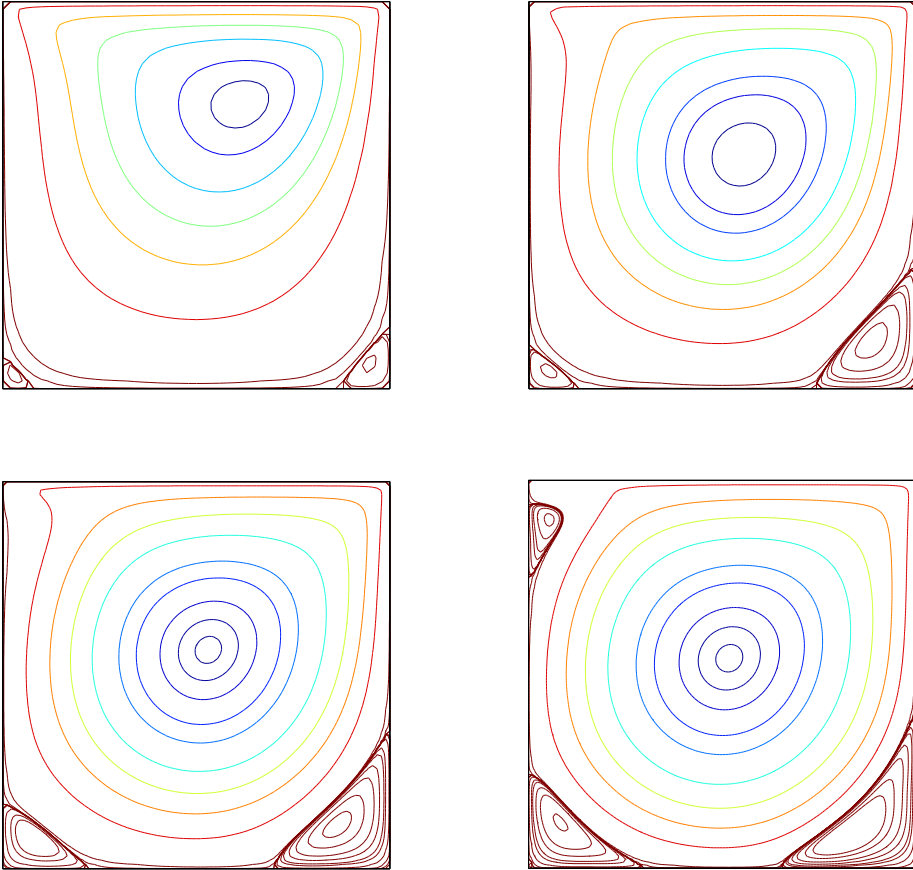
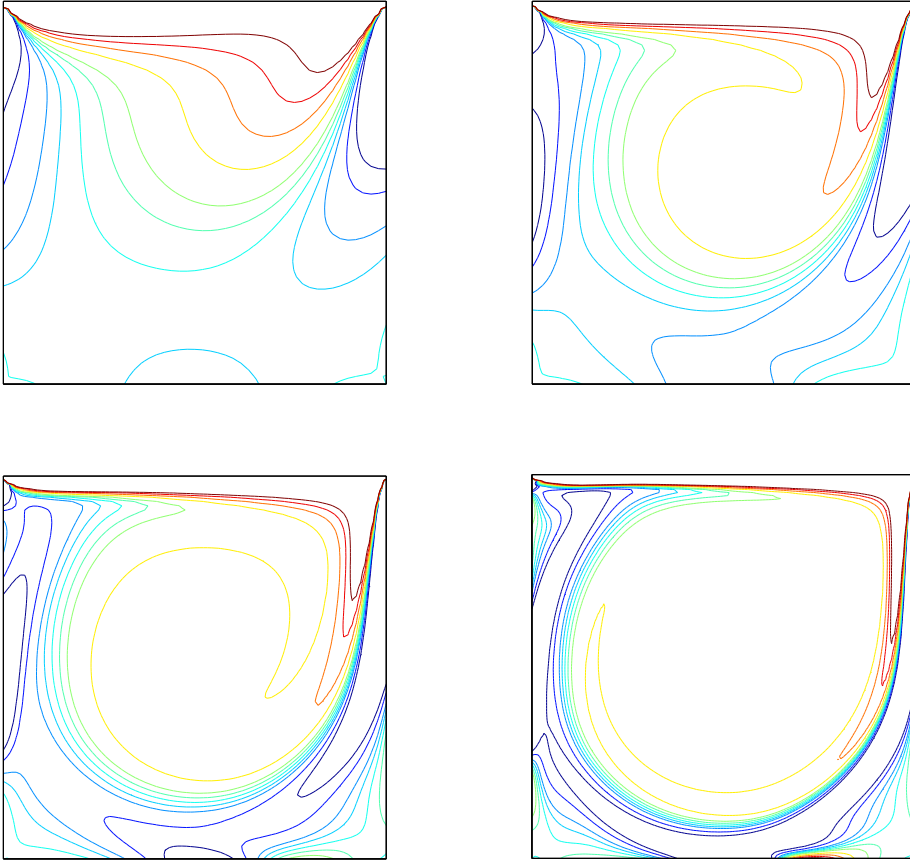Figure 11: Lid driven cavity: Streamlines of the flow for $Re = 100$ (top-left), $Re = 400$ (top-right), $Re = 1000$ (bottom-left), and $Re = 3200$ (bottom-right) with the grid of 51×51, 71×71, 91×91, and 129×129, respectively. The contour values used here are taken to be the same as those in [Ghia, Ghia, and Shin (1982)].

5.6 Irregular bottom lid driven cavity

The lid driven cavity with a deformed base presented in [Udaykumar, Shyy, and Rao (1996); Shyy, Udaykumar, Rao, and Smith (1996)] is chosen to validate the performance of the present fluid flow solver in an irregular domain. The base is deformed sinusoidally with an amplitude of 10 percent of the base. The computational domain and boundary conditions are illustrated in Figure 14. The inte-

Figure 12: Lid driven cavity: Iso-vorticity lines of the flow for $Re = 100$ (top-left), $Re = 400$ (top-right), $Re = 1000$ (bottom-left), and $Re = 3200$ (bottom-right) with the grid of 51×51, 71×71, 91×91, and 129×129, respectively. The contour values used here are taken to be the same as those in [Ghia, Ghia, and Shin (1982)].

rior and boundary nodes are generated in a similar manner described in Section 5.2. The spatial discretisation is shown in Figure 15. A range of uniform grids, $\{53 \times 53, 63 \times 63, 83 \times 83, 93 \times 93\}$ is employed in the simulation. A fixed time step and Reynolds number are chosen to be $\Delta t = 0.001$ and $Re = 1000$, respectively. The results from the present method are compared with those presented in [Shyy, Udaykumar, Rao, and Smith (1996); Mariani and Prata (2008)], where appropriate. From the literature, the FVM (Finite Volume Method) results using the well-tested
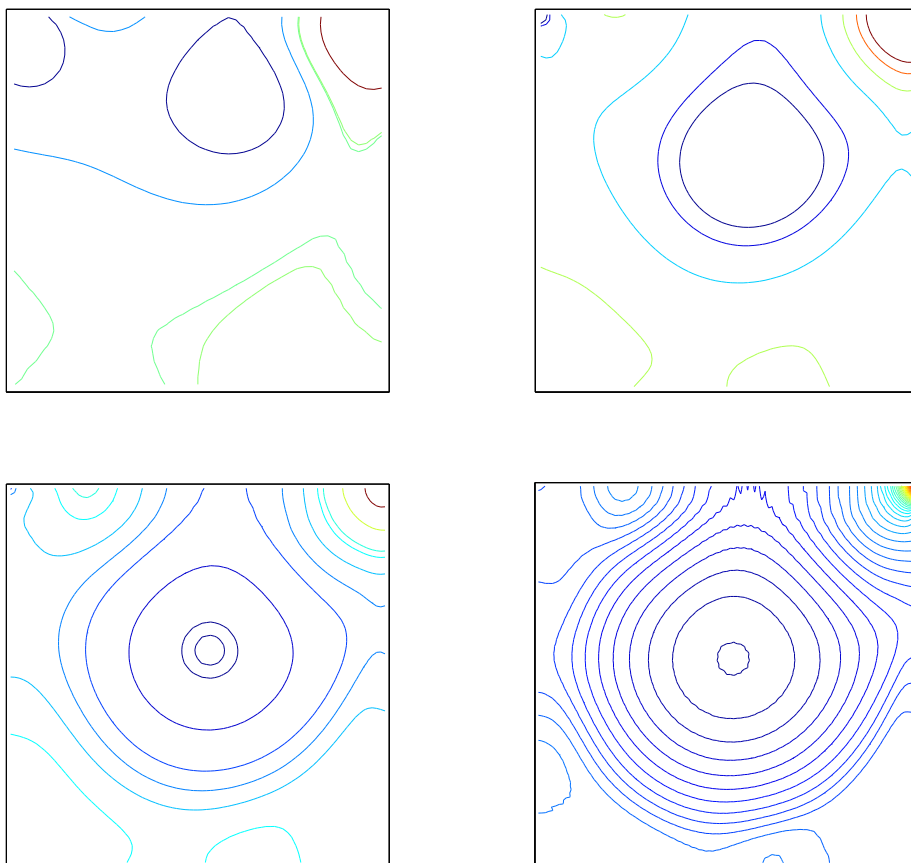
Figure 13: Lid driven cavity: Static pressure contours of the flow for $Re = 100$ (top-left), $Re = 400$ (top-right), $Re = 1000$ (bottom-left), and $Re = 3200$ (bottom-right) with the grid of 51×51, 71×71, 91×91, and 129×129, respectively. The contour values used here are taken to be the same as those in [Abdallah (1987)] for $Re = 100$ and $Re = 400$, [Botella and Peyret (1998)] for $Re = 1000$, and [Bruneau and Saad (2006)] for $Re = 3200$.

body-fitted coordinate formulation and dense grid of 121×121 presented in [Shyy, Udaykumar, Rao, and Smith (1996)] have been considered as "Benchmark" results for comparison purposes.

Figure 16 displays horizontal and vertical velocity profiles along the vertical centreline for different grid sizes at $Re = 1000$, where a grid convergence of the present
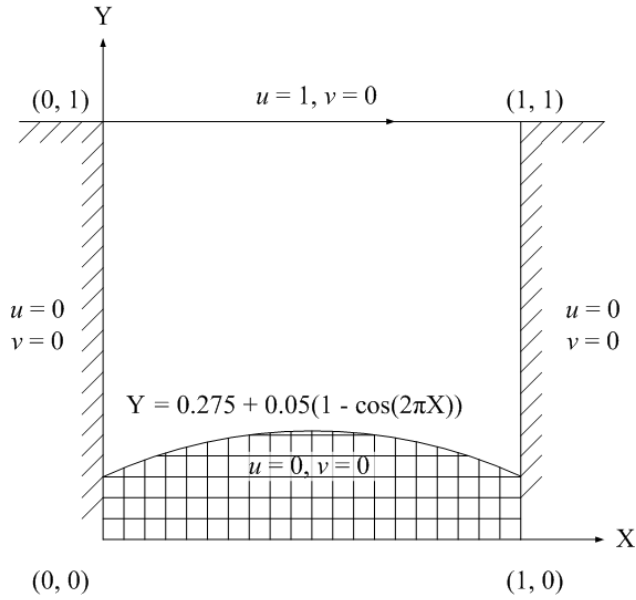
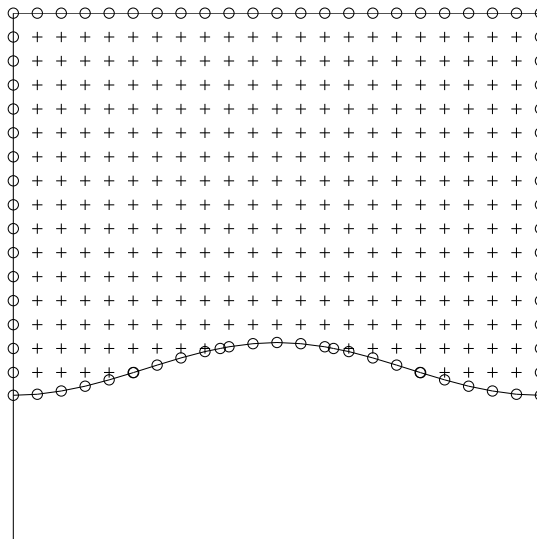Figure 14: Irregular bottom lid driven cavity: problem configuration and boundary conditions.

Figure 15: Irregular bottom lid driven cavity, spatial discretisation: $+$, interior nodes; $\circ$, boundary nodes.
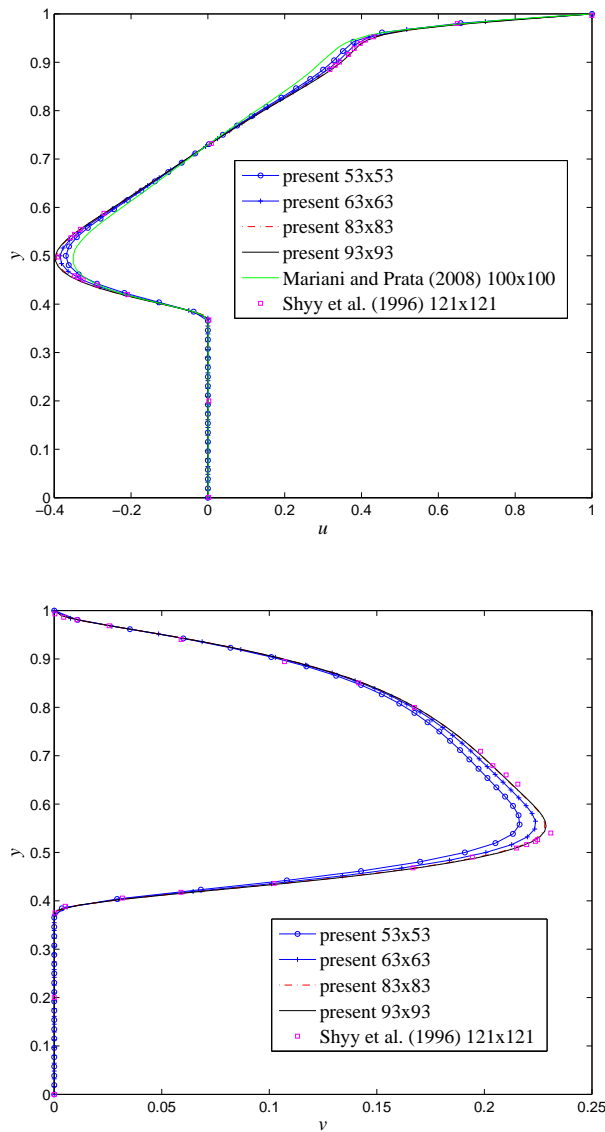
Figure 16: Irregular bottom lid driven cavity, $Re = 1000$: Profiles of the u-velocity (top) and v-velocity (bottom) along the vertical centreline as grid density increases. It is noted that the curves for the last two grids are indistinguishable and in good agreement with the benchmark results of Shyy, Udaykumar, Rao, and Smith (1996).
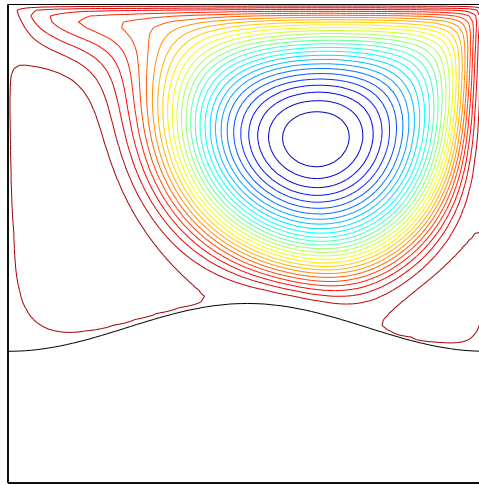
Figure 17: Irregular bottom lid driven cavity: Streamlines of the flow for $Re = 1000$ with the grid of 83×83. The plot contains 30 contour lines whose levels vary linearly from the minimum to maximum values; and, it is in good agreement with that of Shyy, Udaykumar, Rao, and Smith (1996).
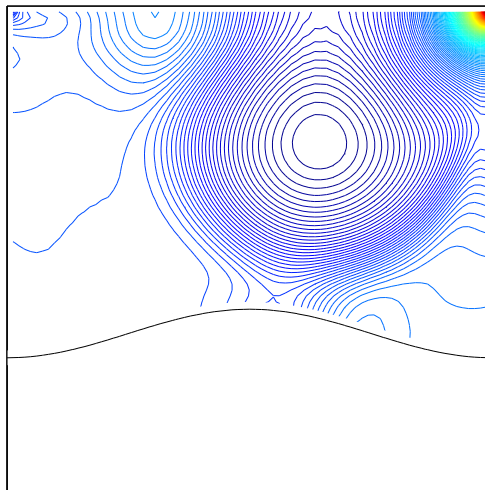

Figure 18: Irregular bottom lid driven cavity: Static pressure contours of the flow for $Re = 1000$ with the grid of 83×83. The plot contains 160 contour lines whose levels vary linearly from the minimum to maximum values.

scheme is obviously observed (i.e. the present solution approaches the benchmark solution with a fast rate as the grid density is increased). The present scheme effectively achieves the benchmark results with a grid of only 83×83 in comparison with the grid of 121×121 used to obtain the benchmark results in [Shyy, Udaykumar, Rao, and Smith (1996)]. In addition, the present results with a grid of only 53×53 outperform those of Mariani and Prata (2008) using the grid of 100×100. To exhibit contour plots of the flow, we employ the grid of 83×83 for $Re = 1000$. Figure 17 shows streamlines which are derived from the velocity field. Figure 18 shows the pressure deviation contours of the present simulation. These plots are in close agreement with those reported in the literature.

6   Concluding remarks

In this paper, we implement the high-order compact integrated radial basis function (CIRBF) scheme, where first- and second-order derivative values of the field variables are included, in combination with the direct fully coupled velocity-pressure approach in the Cartesian-grid point-collocation structure. Like FDMs, the present approximation technique involves 3 nodes in each direction, which results in a sparse system matrix. Numerical examples indicate that the results of the present scheme are superior to those of the standard FDM scheme and second- and fourth-order compact FDM schemes in terms of solution accuracy and convergence rates with grid refinement. It is shown that the CIRBF scheme has at least fourth-order accuracy when approximating the Poisson equations in either rectangular or non-rectangular domains. The combination of the CIRBF and the direct fully coupled approach maintains the fourth-order accuracy in solving the transient flow problems of Taylor-Green vortices in rectangular/non-rectangular domains. In the fluid flow simulations with regular/irregular boundaries, the numerical results obtained by the present approach are highly accurate and in good agreement with the reported results in the literature.

References

Abdallah, S. (1987):   Numerical solutions for the incompressible Navier-Stokes equations in primitive variables using a non-staggered grid, Part II.   *J. Comput. Phys.*, vol. 70, pp. 193–202.

Acharya, S.; Baliga, B.; Karki, K.; Murthy, J.; Prakash, C.; Vanka, S. (2007): Pressure-based finite-volume methods in computational fluid dynamics. *J. Heat Transfer*, vol. 129, pp. 407–424.

Ammara, I.; Masson, C. (2004): Development of a fully coupled control-volume finite element method for the incompressible Navier-Stokes equations. *Int. J. Numer. Meth. Fluids*, vol. 44, pp. 621–644.

Botella, O.; Peyret, R. (1998): Benchmark spectral results on the lid-driven cavity flow. *Comput. Fluids*, vol. 27, no. 4, pp. 421–433.

Braaten, M.; Patankar, S. (1990): Fully coupled solution of the equations for incompressible recirculating flows using a penalty-function finite-difference formulation. *Comput. Mech.*, vol. 6, pp. 143–155.

Braaten, M.; Shyy, W. (1986): Comparison of iterative and direct solution methods for viscous flow calculations in body-fitted co-ordinates. *Int. J. Numer. Meth. Fluids*, vol. 6, pp. 325–349.

Bruneau, C.; Jouron, C. (1990): An efficient scheme for solving steady incompressible Navier-Stokes equations. *J. Comput. Phys.*, vol. 89, pp. 389–413.

Bruneau, C.; Saad, M. (2006): The 2D lid-driven cavity problem revisited. *Comput. Fluids*, vol. 35, pp. 326–348.

Caretto, L.; Curr, R.; Spalding, D. (1972): Two numerical methods for three-dimensional boundary layers. *Comput. Method. Appl. Mech. and Engrg.*, vol. 1, pp. 39–57.

Darwish, M.; Sraj, I.; Moukalled, F. (2009): A coupled finite volume solver for the solution of incompressible flows on unstructured grids. *J. Comput. Phys.*, vol. 228, pp. 180–201.

Deng, G.; Piquet, J.; Queutey, P.; Visonneau, M. (1994a): A new fully coupled solution of the Navier-Stokes equations. *Int. J. Numer. Meth. Fluids*, vol. 19, pp. 605–639.

Deng, G.; Piquet, J.; Queutey, P.; Visonneau, M. (1994b): Incompressible-flow calculations with a consistent physical interpolation finite-volume approach. *Comput. Fluids*, vol. 23, no. 8, pp. 1029–1047.

Elman, H.; Howle, V.; Shadid, J.; Tuminario, R. (2003): A parallel block multi-level preconditioner for the 3D incompressible Navier-Stokes equations. *J. Comput. Phys.*, vol. 187, pp. 504–523.

Fasshauer, G. (2007): *Meshfree approximation methods with Matlab*. World Scientific Publishing, 5 Toh Tuck Link, Singapore 596224.

Furuichi, M.; May, D.; Tackley, P. (2011):   Development of a Stokes flow solver robust to large viscosity jumps using a Schur complement approach with mixed precision arithmetic. *J. Comput. Phys.*, vol. 230, pp. 8835–8851.

Galpin, P.; Doormaal, J. V.; Raithby, G. (1985):   Solution of the incompressible mass and momentum equations by application of a coupled equation line solver. *Int. J. Numer. Meth. Fluids*, vol. 5, pp. 615–625.

Gamet, L.; Ducros, F.; Nicoud, F.; Poinsot, T. (1999):   Compact finite difference schemes on non-uniform meshes. Application to direct numerical simulations of compressible flows. *Int. J. Numer. Meth. Fluids*, vol. 29, pp. 159–191.

Ghia, U.; Ghia, K.; Shin, C. (1982):   High-resolutions for incompressible flows using Navier-Stokes equations and a multigrid method. *J. Comput. Phys.*, vol. 48, pp. 387–411.

Gresho, P.; Chan, S.; Lee, R.; Upson, C. (1984):   A modified finite element method for solving the time-dependent, incompressible Navier-Stokes equations. Part 2: Applications. *Int. J. Numer. Meth. Fluids*, vol. 4, pp. 619–640.

Hanby, R.; Silvester, D.; Chew, J. (1996):   A comparison of coupled and segregated iterative solution techniques for incompressible swirling flow. *Int. J. Numer. Meth. Fluids*, vol. 22, pp. 353–373.

Henniger, R.; Obrist, D.; Kleiser, L. (2010):   High-order accurate solution of the incompressible Navier-Stokes equations on massively parallel computers. *J. Comput. Phys.*, vol. 229, pp. 3543–3572.

Kansa, E. (1990a):   Multiquadrics-A scattered data approximation scheme with applications to Computational Fluid-Dynamics-I. Surface approximations and partial derivative estimates. *Computers Math. Appfic.*, vol. 19, no. 8/9, pp. 127–145.

Kansa, E. (1990b):   Multiquadrics-A scattered data approximation scheme with applications to Computational Fluid-Dynamics-II. Solutions to parabolic, hyperbolic and elliptic partial differential equations. *Computers Math. Appfic.*, vol. 19, no. 8/9, pp. 147–161.

Karki, K.; Mongia, H. (1990):   Evaluation of a coupled solution approach for fluid flow calculations in body-fitted co-ordinates. *Int. J. Numer. Meth. Fluids*, vol. 11, pp. 1–20.

Mai-Duy, N.; Tanner, R. (2007):   A collocation method based on one-dimensional RBF interpolation scheme for solving PDEs. *Int. J. Numer. Meth. Heat Fluid Flow*, vol. 17, no. 2, pp. 165–186.

Mai-Duy, N.; Tran-Cong, T. (2001a):   Numerical solution of differential equations using multiquadric radial basis function networks. *Neural Networks*, vol. 14, pp. 185–199.

Mai-Duy, N.; Tran-Cong, T. (2001b):   Numerical solution of Navier-Stokes equations using multiquadric radial basis function networks. *Int. J. Numer. Meth. Fluids*, vol. 37, pp. 65–86.

Mai-Duy, N.; Tran-Cong, T. (2003):   Approximation of function and its derivatives using radial basis function networks. *Appl. Math. Modell.*, vol. 27, pp. 197–220.

Mai-Duy, N.; Tran-Cong, T. (2005):   An efficient indirect RBFN-based method for numerical solution of PDEs. *Numer. Methods Partial. Diff. Equations*, vol. 21, no. 4, pp. 770–790.

Mai-Duy, N.; Tran-Cong, T. (2007):   A Cartesian-grid collocation method based on radial basis-function networks for solving PDEs in irregular domains. *Numer. Methods Part. Differ. Eqs.*, vol. 23, pp. 1192–1210.

Mai-Duy, N.; Tran-Cong, T. (2010):   A numerical study of 2D integrated RBFNs incorporating Cartesian grids for solving 2D elliptic differential problems. *Numer. Methods Part. Differ. Eqs.*, vol. 26, no. 6, pp. 1443–1462.

Mai-Duy, N.; Tran-Cong, T. (2013):   A compact five-point stencil based on integrated RBFs for 2D second-order differential problems. *J. Comput. Phys.*, vol. 235, pp. 302–321.

Mariani, V.; Prata, A. (2008):   A Eulerian-Lagrangian method applied to fluid flow in lid-driven cavities with irregular bottom walls. *Numer. Heat Tr. B-Fund.*, vol. 53, pp. 206–233.

May, D.; Moresi, L. (2008):   Preconditioned iterative methods for Stokes flow problems arising in computational geodynamics. *Phys. Earth Planet. In.*, vol. 171, pp. 33–47.

Mazhar, Z. (2001):   A procedure for the treatment of the velocity-pressure coupling problem in incompressible fluid flow. *Numer. Heat Tr. B-Fund.*, vol. 39, pp. 91–100.

Moin, P.; Kim, J. (1980):   On the numerical solution of time-dependent viscous incompressible fluid flows involving solid boundaries. *J. Comput. Phys.*, vol. 35, pp. 381–392.

Pascau, A.; Perez, C. (1996):   A comparison of segregated and coupled methods for the solution of the incompressible Navier-Stokes equations. *Commun. Numer. Meth. Engrg.*, vol. 12, pp. 617–630.

Patankar, S.; Spalding, D. (1972):   A calculation procedure for heat, mass and momentum transfer in three-dimensional parabolic flows. *Int. J. Heat Mass Transfer*, vol. 15, pp. 1767–1806.

Perot, J. (1993):   An analysis of the fractional step method.   *J. Comput. Phys.*, vol. 108, pp. 51–58.

Sahin, M.; Owens, R. (2003):   A novel fully implicit finite volume method applied to the lid-driven cavity problem - Part I: High Reynolds number flow calculations. *Int. J. Numer. Meth. Fluids*, vol. 42, pp. 57–77.

Shyy, W.; Udaykumar, H.; Rao, M.; Smith, R. (1996):   *Computational fluid dynamics with Moving boundaries*. Taylor&Francis, 1900 Frost Road, Suite 101, Bristol, PA 19007-1598.

Silvester, D.; Elman, H.; Kay, D.; Wathen, A. (2001):   Efficient preconditioning of the linearized Navier-Stokes equations for incompressible flow.   *J. Comput. Appl. Math.*, vol. 128, pp. 261–279.

Thai-Quang, N.; Le-Cao, K.; Mai-Duy, N.; Tran-Cong, T. (2012):   A high-order compact local integrated-RBF scheme for steady-state incompressible viscous flows in the primitive variables.   *CMES: Computer Modeling in Engineering and Sciences*, vol. 84, no. 6, pp. 528–557.

Thai-Quang, N.; Mai-Duy, N.; Tran, C.-D.; Tran-Cong, T. (2012):   High-order alternating direction implicit method based on compact integrated-RBF approximations for unsteady/steady convection-diffusion equations.   *CMES: Computer Modeling in Engineering and Sciences*, vol. 89, no. 3, pp. 189–220.

Tian, Z.; Liang, X.; Yu, P. (2011):   A higher order compact finite difference algorithm for solving the incompressible Navier-Stokes equations.   *Int. J. Numer. Meth. Engng.*, vol. 88, no. 6, pp. 511–532.

Udaykumar, H.; Shyy, W.; Rao, M. (1996):   ELAFINT: A mixed Eulerian-Lagrangian method for fluid flows with complex and moving boundaries.   *Int. J. Numer. Meth. Fluids*, vol. 22, pp. 691–712.

Uhlmann, M. (2005):   An immersed boundary method with direct forcing for the simulation of particular flows.   *J. Comput. Phys*, vol. 209, pp. 448–476.

Vanka, S. (1986a):   Block-implicit multigrid solution of Navier-Stokes equations in primitive variables.   *J. Comput. Phys.*, vol. 65, pp. 138–158.

Vanka, S. (1986b):   A calculation procedure for three-dimensional steady recirculating flows using multigrid methods.   *Comput. Method. Appl. Mech. and Engrg.*, vol. 55, pp. 321–338.

Zedan, M.; Schneider, G. (1985):   A coupled strongly implicit procedure for velocity and pressure computation in fluid flow problems.   *Numer. Heat Transfer*, vol. 8, pp. 537–557.